

Enhanced elastomer-like auxetic cementitious materials through strain-hardening cementitious composites (SHCC) with extended softening properties

Xie, Jinbao; He, Shan; Xu, Yading; Meng, Zhaozheng; Zhou, Wen; Schlangen, Erik; Šavija, Branko

DOI

[10.1016/j.cemconcomp.2025.106069](https://doi.org/10.1016/j.cemconcomp.2025.106069)

Publication date

2025

Document Version

Final published version

Published in

Cement and Concrete Composites

Citation (APA)

Xie, J., He, S., Xu, Y., Meng, Z., Zhou, W., Schlangen, E., & Šavija, B. (2025). Enhanced elastomer-like auxetic cementitious materials through strain-hardening cementitious composites (SHCC) with extended softening properties. *Cement and Concrete Composites*, 161, Article 106069. <https://doi.org/10.1016/j.cemconcomp.2025.106069>

Important note

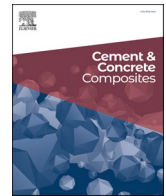
To cite this publication, please use the final published version (if applicable). Please check the document version above.

Copyright

Other than for strictly personal use, it is not permitted to download, forward or distribute the text or part of it, without the consent of the author(s) and/or copyright holder(s), unless the work is under an open content license such as Creative Commons.

Takedown policy

Please contact us and provide details if you believe this document breaches copyrights. We will remove access to the work immediately and investigate your claim.



Enhanced elastomer-like auxetic cementitious materials through strain-hardening cementitious composites (SHCC) with extended softening properties

Jinbao Xie , Shan He ^{*} , Yading Xu , Zhaozheng Meng , Wen Zhou , Erik Schlangen , Branko Šavija 

MicroLab, Faculty of Civil Engineering and Geosciences, Delft University of Technology, Delft, 2628CN, the Netherlands

ARTICLE INFO

Keywords:

Auxetic cementitious cellular composites
Additive manufacturing
Strain-hardening cementitious composites
Elastomer-like cementitious materials
Compressive resilience
Softening

ABSTRACT

Auxetic cementitious cellular composites (ACCCs) exhibit hinge-type recoverable deformation during auxetic behavior phase, a rare pseudo-elastic property in cementitious materials. However, their low load-bearing capacity during this phase restricts their use in high-load applications. This study developed ACCCs using strain-hardening cementitious composites (SHCCs) with short (SHCC-SS) and long (SHCC-LS) softening tails, fabricated by additive manufacturing-assisted casting. Uniaxial compression tests employing Digital Image Correlation (DIC) evaluated their compressive behavior, peak strength, Poisson's ratio variation, and energy dissipation. Cyclic tests after pre-compression assessed their recoverable deformation resilience, with fiber bridging at joint cracks examined using digital optical microscope. Results were compared to a reference using fiber-reinforced cementitious materials with strain softening (SS). Compared to the reference (SS), ACCCs using SHCC mixtures exhibit superior load-bearing capacity and stable auxetic behavior under compression. After self-contact, they maintain a negative Poisson's ratio up to a considerably high compressive strain, preventing splitting failure and preserving structural integrity. This is because incorporating SHCC enables greater joint rotation by promoting multiple cracks with strain hardening, which delays primary crack formation and reduces its opening. During cyclic tests, P1-shaped ACCCs with SHCC-LS and SHCC-SS enhance the elasticity modulus of recoverable deformation by 4.8 and 3.0 times, respectively, compared to SS. SHCC-LS outperforms SHCC-SS in compressive resilience due to its prolonged softening tail, which improves fiber bridging in primary cracks and increases rotational stiffness in hinge joints. SHCC mixtures with initial strain hardening and extended softening enable scalable design of advanced auxetic cementitious materials across various load levels.

1. Introduction

Additive manufacturing of cement-based materials enables the development of Architected Cement-based Materials (ACMs), which incorporate intricately designed internal geometries on a millimeter to centimeter scale. These geometries are tailored to achieve specific mechanical properties. Typically, ACMs are composed of repeated unit cells, where the overall bulk properties depend on both the mesoscale geometry of the unit cells and the characteristics of the matrix material. Moini et al. [1] employed 3D printing technology to produce solidified cement paste elements, developing bioinspired Bouligand architectures recognized for their resilient properties and advanced performance

characteristics. Sajadi et al. [2] employed cementitious materials to create schwarzite structures through the use of 3D-printed molds, significantly improving the ductility, toughness, and energy absorption capabilities of cement-based materials. Wan et al. [3] utilized direct ink writing to manufacture cementitious materials capable of self-healing through vascular networks created by incorporating purposeful hollow channels within the cement matrix. This pioneering approach allows for construction materials with mechanical tunability and advanced functionalities, marking a crucial step toward reimagining traditional civil infrastructure systems. Further, these architected cementitious structures are lightweight and less dense than solid materials, leading to reduced material usage. By reducing the use of cement, this approach is

* Corresponding author.

E-mail addresses: J.Xie-1@tudelft.nl (J. Xie), S.He-2@tudelft.nl (S. He), yadingx@gmail.com (Y. Xu), Z.Meng@tudelft.nl (Z. Meng), w.zhou-2@tudelft.nl (W. Zhou), Erik.Schlangen@tudelft.nl (E. Schlangen), B.Savija@tudelft.nl (B. Šavija).

<https://doi.org/10.1016/j.cemconcomp.2025.106069>

Received 22 November 2024; Received in revised form 20 March 2025; Accepted 27 March 2025

Available online 10 April 2025

0958-9465/© 2025 The Author(s). Published by Elsevier Ltd. This is an open access article under the CC BY license (<http://creativecommons.org/licenses/by/4.0/>).

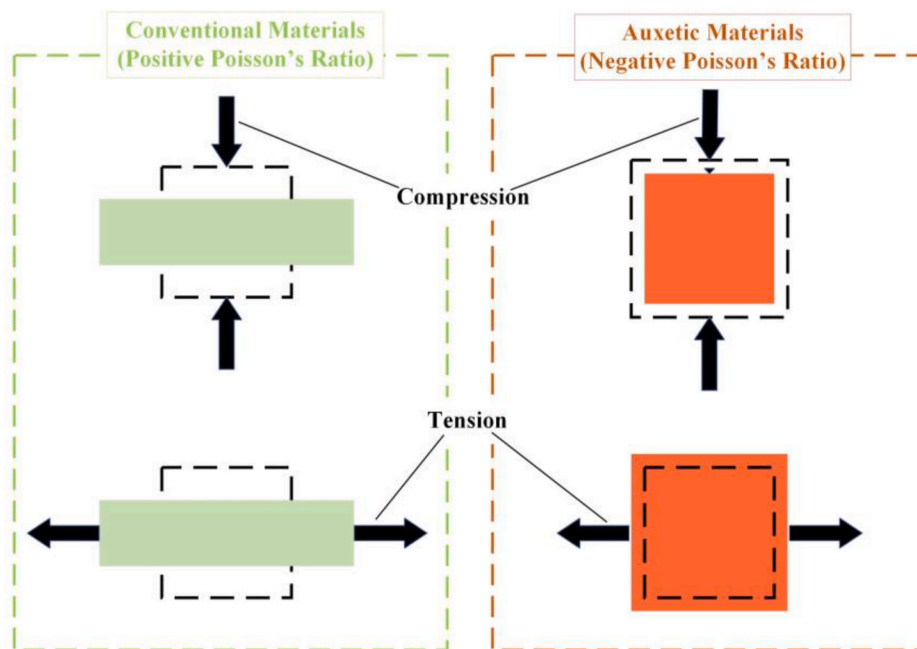
also cost-effective and helps lower carbon emissions, as cement production is a major source of CO₂.

Plain cementitious materials have long been criticized for their brittleness, making them susceptible to cracking even under minor deformations. To address this issue, reinforced cementitious composites are frequently utilized in both research and engineering. One common approach is to incorporate short fibers to improve the ductility of plain cementitious materials. Through specialized mixture designs, it is possible to achieve strain-hardening behavior under tensile loads, as seen in SHCC [4–9]. This development enables the creation of intricate forms, resulting in a wider variety of structures with improved mechanical properties. Nguyen-Van et al. [10] examined the flexural properties of 3D-printed concrete beams with Bouligand structures, creating a simulation framework to predict anisotropy in steel fiber-reinforced materials. Liu et al. [11] studied 3D-printed fibre-reinforced concrete with a Bouligand helical pattern under impact stress and found that the pitch angle greatly influences impact resistance. Inspired by the mantis shrimp in nature, Du et al. [12] utilized Bouligand structures to enhance 3DP-Strain-Hardening Cementitious Composites (3DP-SHCC). Inspired by conch shells in nature, Zhou et al. [13] used innovative "knitting" and "tilting" filament printing patterns to enhance the bending performance and reduce the anisotropy of 3D-printed ECCs. Ohno et al. [14] created a design framework for truss-type ACMs utilizing SHCC, with an emphasis on maximizing energy absorption during compression. In our previous study [15], we used an "indirect" 3D printing technique to create ACCCs. This involved 3D printing negative molds from materials like ABS to efficiently produce silicone rubber molds for casting uniquely shaped cementitious materials.

Conventional materials have positive Poisson's ratios, expanding laterally under compression and contracting laterally under tension, as shown in Fig. 1. In contrast, auxetic materials have negative Poisson's ratios, contracting laterally under compression and expanding laterally under tension. For auxetic concrete, Xu et al. [15] developed auxetic concrete by using a fiber-reinforced cementitious composite as the base material and designing a cellular structure with evenly distributed elliptical voids. This structure is referred to as elliptical-shaped ACCCs. Xie et al. [16] developed peanut-shaped ACCCs to enhance energy

dissipation capability, ductility, and toughness by mitigating stress concentration through the incorporation of peanut-shaped holes. Under uniaxial compression, the ACCCs exhibited auxetic behavior with a negative Poisson's ratio due to the crack bridging mechanism within the cementitious matrix. The lateral contraction densified the material and enhanced its resistance to splitting failure. Additionally, this inward lateral pull increased material deformation, leading to higher energy absorption. Meanwhile, the increased porosity of auxetic structures reduces their mass, showcasing the potential of ACCCs as lightweight, high-performance structural materials. Xu et al. [17] further developed a 3D auxetic cementitious-polymeric composite (3D-ACPC) with a 3D-printed polymer shell and cementitious mortar, exhibiting compressive strain-hardening and high energy absorption. Additionally, incorporating 3D-printed polymeric auxetic reinforcement structures into cementitious mortar produces composites with enhanced properties [18–20]. These composites demonstrate significant compressive ductility, high recoverable deformability, and superior energy dissipation due to the synergistic effects of the auxetic structures combined with the mortar.

Typically, ACCCs exhibit two distinct stages with two peak stress points under uniaxial compression, marked by the strain at which self-contact occurs within the central hole between the top and bottom ends (i.e., the self-contact point). In Fig. 2, ACCCs begin to display a higher magnitude of negative Poisson's ratio (high auxetic behavior) after the first peak stress in Stage I. Upon reaching the self-contact point, the magnitude of the negative Poisson's ratio starts to decrease until it reaches zero and then becomes a positive Poisson's ratio during Stage II. The range from the first peak stress point to the self-contact point represents a compressive strain range characterized by high auxetic behavior. Within this range, ACCCs demonstrate significant deformation capacity and a certain level of recoverable elastic deformation—a pseudo-elastic characteristic not typically found in traditional cementitious materials. The remarkable recoverable deformation behavior of ACCCs, akin to elastomers, broadens the potential applications of elastomer-like cementitious materials. They can be employed to create advanced multifunctional cementitious composites, incorporating features such as mechanical tunability, energy harvesting, and sensing capabilities. Xie et al. [21] have leveraged this innovative capability for



Note: Dashed box represents the original state.

Fig. 1. Schematic diagrams illustrating positive (a) and negative (b) Poisson's ratios in bulk materials.

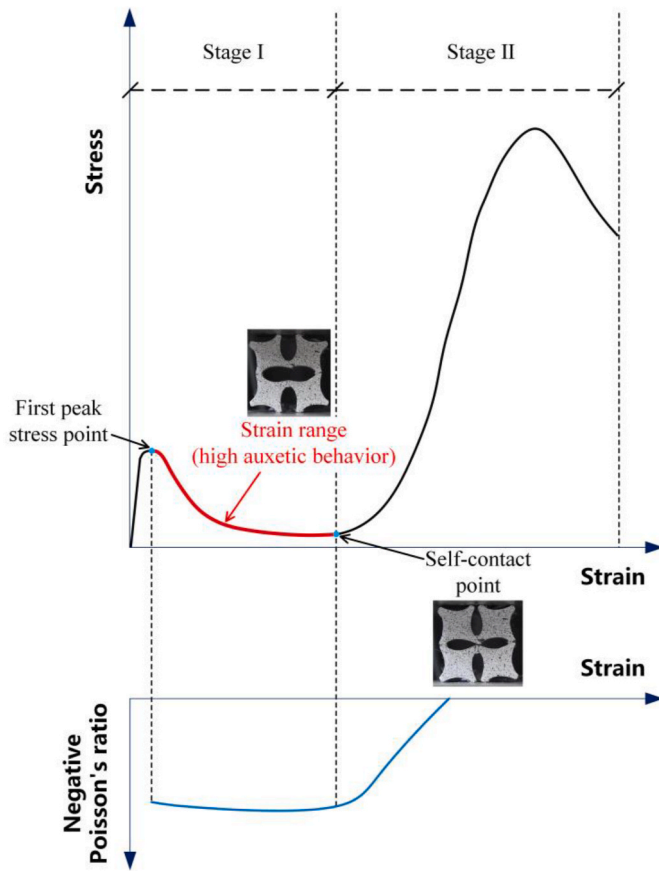


Fig. 2. Strain range with high auxetic behavior during uniaxial compression.

energy harvesting by integrating PVDF (Polyvinylidene Fluoride) into ACCCs. Energy harvesting experiments have shown that the ACCCs-PVDF system generates a sinusoidal output voltage with peaks reaching several volts during each cycle of cyclic loading. Barri et al. [22] integrated concrete mixture with graphite powder and auxetic polymer structures, resulting in a concrete material system that exhibits unprecedented mechanical and electrical tunability due to snap-through buckling behavior. Valverde-Burneo [23] has developed a multifunctional cementitious material reinforced with PVA and recycled carbon fibers. This material exhibits both conductive and auxetic properties, making it suitable for applications such as self-sensing concrete. However, the compressive strain range with high auxetic behavior tends to result in low stress from crack bridging (i.e., poor load-bearing capacity or stiffness), even though the deformation in this range is significant. This issue limits its applicability in high load-capacity scenarios, such as vehicle loads, making it challenging for engineering applications. Additionally, low rotational stiffness, due to poor fiber-bridging and a single widened crack in the joints, is more prone to damage, particularly considering the heterogeneity of cementitious materials [24–27] and inconsistencies in manual casting quality.

This study aimed to improve the load-bearing capacity and recoverable deformation elasticity of ACCCs within their high auxetic behavior range by using SHCC. Elliptical ACCCs were designed and fabricated using two types of SHCC—one with short softening tail and one with long softening tail—through additive manufacturing-assisted casting. The ACCC specimens underwent uniaxial compression tests combined with DIC to evaluate their compressive behavior, peak strength, Poisson's ratio variation, and energy dissipation capacity. Following initial compression into the high auxetic behavior range, cyclic tests assessed their compressive deformation resilience. A digital optical microscope was then employed to analyze fiber bridging at the

cracks in the joints between adjacent holes in the ACCCs. Results were compared with a reference mixture of fiber-reinforced cementitious materials with strain softening.

2. Experiments

2.1. Design theory

Fig. 3 gives a schematic illustration of the auxetic mechanism of ACCCs under uniaxial compression. Due to the chirality of each cell section in the studied structure, the joints are misaligned locally. The symmetric structure does not experience shear force at the joints in the middle. When a uniaxial compressive load is applied, these joints undergo a bending moment (indicated in green box) similar to a four-point bending condition (Fig. 3a). This creates tensile stresses (indicated by red arrows) at the two ends of the minor axis and compressive stresses (indicated by blue arrows) at the two ends of the major axis (Fig. 3a). Since cementitious materials are much weaker in tension than in compression, cracks form on the tension side. As shown in Fig. 3b, cementitious matrix without fiber or with insufficient fiber bridging will quickly develop cracks throughout the joint, causing the sections to separate. The auxetic behavior of ACCCs is achieved through section rotation by angle θ around the joints (Fig. 3a) and inward folding at the hollow spaces. The behavior of the cracked specimen depends on the fiber-bridging ability of the cementitious materials. Fiber is added to the cementitious matrix to limit crack development. As illustrated in Fig. 3c, the primary crack develops into a triangular shape under bending. When the crack opens on the tensile side of the joint, the fiber bridging within the crack restricts its growth, preserving the integrity of the compression side of the joint. As a result, the significant deformation in the joints accommodates most of the externally applied compressive strain, thereby reducing the amount of compression in the vertical ligaments and leading to a collective rotational motion and a corresponding decrease in compressive stress. These cracked joints function as hinges, facilitating section rotation and inward folding for auxetic behavior. In Fig. 3c, primarily only one crack forms in the joints of ACCCs during section rotation, and its poor fiber-bridging capacity results in limited rotational stiffness. When considering high load-capacity scenarios (i.e., vehicle load), this makes it difficult to apply in engineering applications. Low rotational stiffness from poor fiber-bridging and a single widened crack is highly vulnerable to damage, especially due to material heterogeneity and manual casting inconsistencies.

The SHCC mixture enables ACCCs to develop multiple cracks in the joints. Instead of one primary crack, these multiple cracks can share and collectively sustain large deformations. This further reduces the opening of the primary crack and maintains effective fiber bridging during the later stages of high auxetic behavior. Typically, SHCC achieves large ductility through the formation of multiple small cracks, each sustaining limited strain. However, when the primary crack forms, it typically fails quickly with shortened softening tail. The significant rotation of ACCCs tends to produce one primary crack in the joints in the later stages, requiring this crack to sustain large deformations through effective fiber bridging. Extending the softening phase after the primary crack forms is expected to maintain effective fiber bridging and support the large deformations required for the auxetic behavior.

The pseudo strain-hardening (PSH) behavior of in SHCC [28–32] was achieved by an energy-based criterion for flat crack propagation (Fig. 3d), which illustrates the relationship between fiber bridging stress (σ) and crack opening (δ). Specially, the crack-tip toughness J_{tip} of the matrix material should be lower than the maximum available complementary energy J_b . The J_{tip} signifies the energy required to fracture the matrix material at the crack tip. The J_b represents the maximum complementary energy, accounting for the upper limit of fiber bridging, which occurs when the peak stress and crack opening reach their maximum values σ_0 and δ_0 . In Fig. 3d, J_{tip} and J_b are represented by the

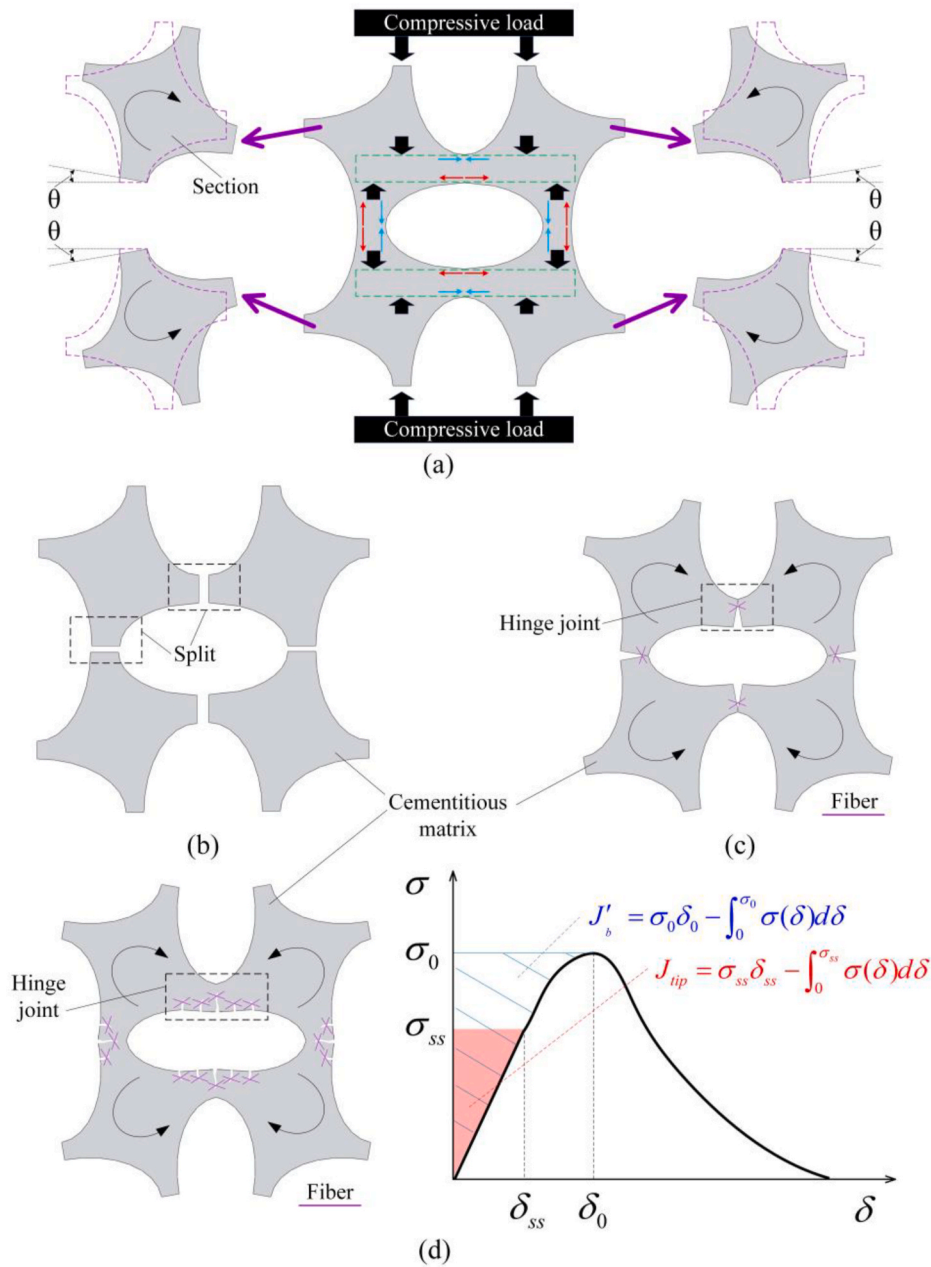


Fig. 3. Auxetic behavior of ACCCs under compression, (a) section rotation, (b) ACCCs without fiber, (c) ACCCs with fiber-bridging in a single crack, (d) ACCCs with fiber-bridging in multiple cracks, and typical σ - δ relationship for fiber bridging in SHCC.

shaded area and the hatched area, respectively.

2.2. Sample preparation

Most auxetic metamaterials with auxetic unit cells are made from polymer or metal materials. These materials exhibit uniform deformation across different unit cells due to their highly homogeneous and ductile nature, which allows for significant deformation. In contrast, ACCCs, which use pseudo-brittle cementitious materials, are more susceptible to additional factors such as manual casting uncertainties, material heterogeneity, and loading boundary conditions (e.g., friction at the contact surface between the specimen and the loading plate). To more accurately assess the effect of constituent material changes on the mechanical performance of ACCCs, a single auxetic unit cell was used in this study. The fabrication of ACCCs followed the "indirect printing" process [33] illustrated in Fig. 4. Firstly, a designed unit cell with the

dimensions was generated using a Fused Deposition Modeling (FDM) 3D printer, specifically the Ultimaker 2+, with ABS as the chosen printing material. The printed ABS shapes were then fixed inside a cardboard box. Subsequently, a two-component silicone rubber, Poly-Sil PS 8510, was mixed in a 1:1 mass ratio and poured into the box. The silicone rubber underwent curing at room temperature for a minimum of 1 h until hardening. Following this, the solidified silicone rubber was extracted from the box, serving as a mold for casting cementitious materials. Table 1 gives the geometric parameters of P1-shaped ACCCs, which was designed in our previous study [16].

2.3. Mixture design

A fine-grained fiber-reinforced mortar was used as the constituent material for ACCCs, with the mixture proportions shown in Table 2. Based on the design theory outlined in Section 2.1, three mixtures were

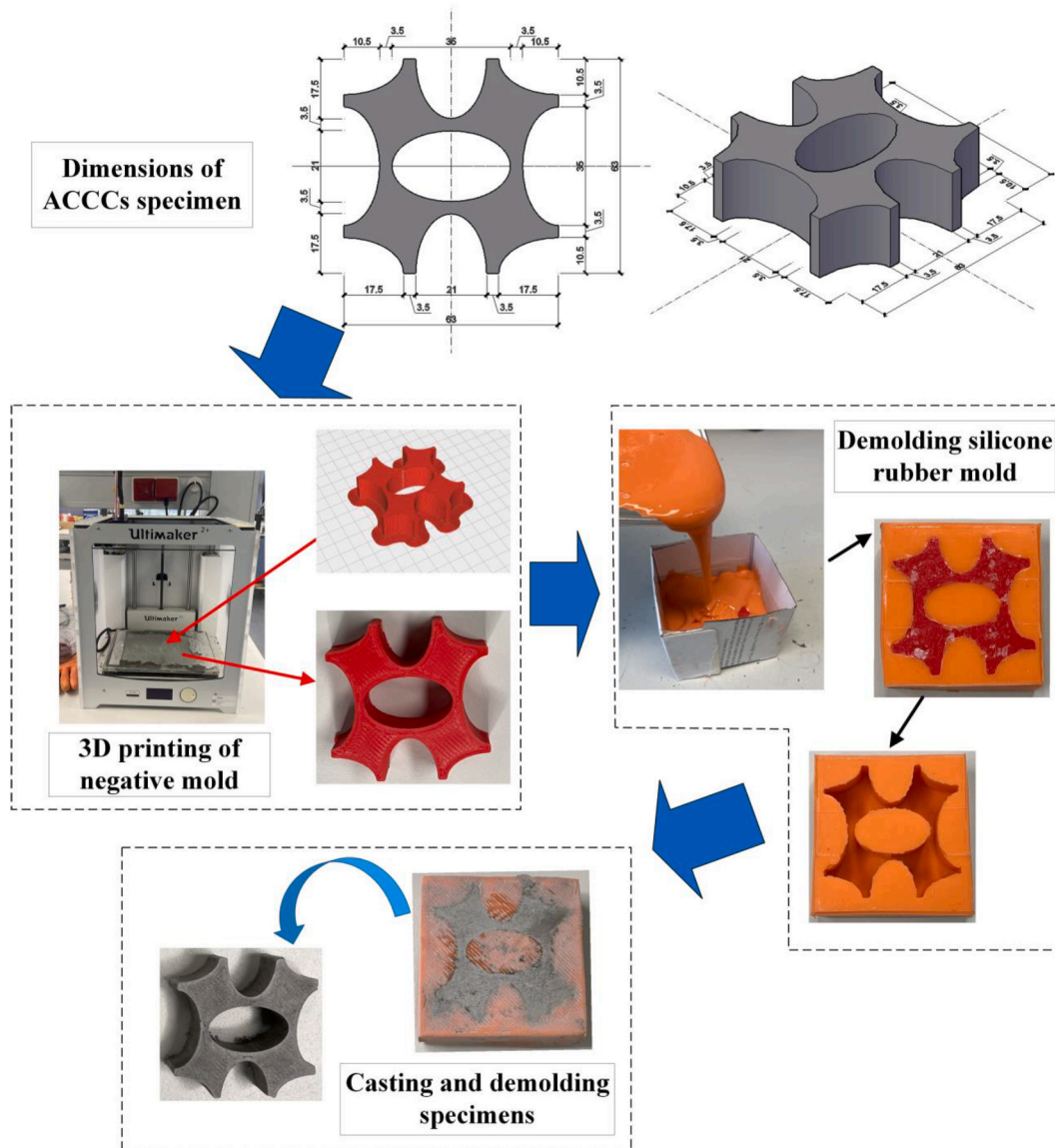


Fig. 4. Procedures for manufacturing ACCCs specimen.

Table 1
Design geometric parameters of P1-shaped ACCCs specimen.

Major axis (mm)	Minor axis (mm)	Aspect ratio	One Ellipse area (mm ²)	Specimen side length (mm)	Specimen thickness (mm)	Specimen volume (cm ³)	Relative density
35.0	21.0	1.67	577.27	63	20	33.20	41.82 %

Table 2
Mixtures used in this study (by weight).

Label	C	FA	S/(C + FA)	W/(C + FA)	SP/(C + FA)	VMA/(C + FA)	PVA(Reference) (by volume)	PVA(RECS15) (by volume)
SS	1.0	1.2	0.37	0.46	0.0016	0.0003	2 %	-
SHCC-LS	1.0	1.2	0.37	0.46	0.0016	0.0003	-	2 %
SHCC-SS	1.0	2.2	0.26	0.32	0.0083	0.0003	-	2 %

designed to achieve the target uniaxial tensile stress-strain curves shown in Fig. 5. Mixture SS (reference) represents strain softening behavior after reaching peak stress, as similarly used in our previous studies [16, 21,33]. Mixture SHCC-SS is a typical SHCC that demonstrates significant strain hardening due to the development of numerous microcracks,

followed by a short softening tail after crack localization occurs in the main crack [4,8,9,34-39]. The SHCC-LS mixture is specifically engineered to improve ductility by exhibiting moderate strain hardening and multiple cracking at the onset, followed by a long softening tail. This extended softening tail enhances fiber bridging within the primary crack

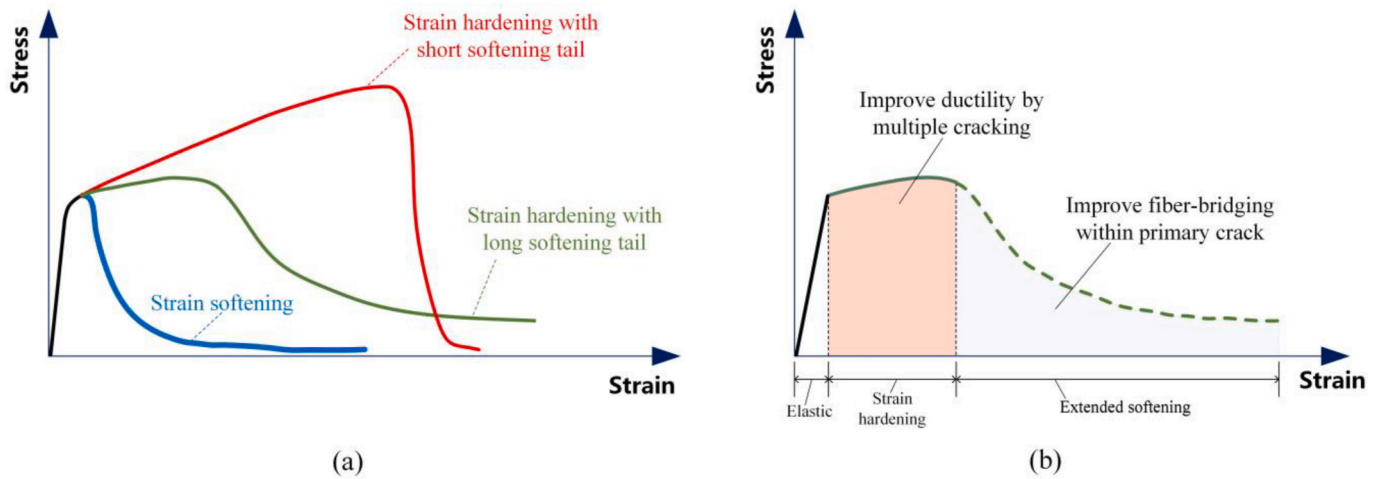


Fig. 5. Uniaxial tensile behavior, (a) three mixtures, (b) SHCC mixture with extended softening.

after crack localization. The ingredients (see Appendix A) included CEM I 42.5 N, fly ash, sand (with a grain size between 125 and 250 μm), water, a polycarboxylate superplasticizer, a viscosity modifying agent (VMA), and Poly-vinyl-alcohol (PVA) fiber. Methylcellulose powder from Shanghai Ying Jia Industrial Development Co. Ltd. was used as a viscosity modifying agent (VMA) to improve fiber distribution. To attain the desired workability, MasterGlenium 51, a polycarboxylate-based superplasticizer from BASF (Germany), was utilized. For the reference mixture (Ref), 2 % volume fraction of Polyvinyl Alcohol (PVA) fiber from Changzhou TianYi Engineering Fiber was used. The two SHCC mixtures were reinforced with 2 % volume fraction of RECS15 PVA fiber from Kuraray GmbH. Fiber specifications are in Table 3.

The dry ingredients—CEM I 42.5, fly ash, sand, and VMA—were combined using a Hobart mixer for 4 min. Then, water and superplasticizer were added to the dry ingredients, followed by an additional 2 min of mixing. Next, fibers were slowly added into the mortar and mixed for another 2 min. The mixture was subjected to high-speed rotation for 5 min to ensure uniform fiber distribution within the matrix. The resulting fresh paste was poured into silicone molds, with each mold being filled in two layers. Each layer was vibrated for 20 s to ensure thorough consolidation. Plastic films were applied to cover the molds to prevent evaporation. After three days of curing at room temperature, the specimens were demolded and transferred to a curing chamber set at 20 °C and 96 % relative humidity, where they remained until reaching 28 days of age.

2.4. Experimental test

As shown in Fig. 6a, uniaxial tensile tests using dog bone specimens, as recommended by the Japan Society of Civil Engineers [40], were conducted to evaluate the tensile behavior of the three mixtures after 28 days of curing. The dimensions of dog bone specimens are illustrated in Fig. 6b, and they were cast using the mold depicted in Fig. 6c. These tests utilized a TREBEL machine under displacement control with a constant loading rate of 0.005 mm/s. The displacement in the gauge region, with a testing volume of 13 × 80 × 30 mm³ (indicated by the blue dashed lines in Fig. 6b), was measured by the linear variable differential transducers (LVDT) positioned on the backside of the specimen. The deformation of the gauge region was also monitored across their entire

area using DIC. DIC involves capturing images with cameras to track and record the surface movement of a deforming solid. The gauge region for DIC measurements were first painted white and then sprayed with a black speckle pattern. During loading, images for DIC were captured every 5 s by using a digital camera. The DIC results were subsequently processed using GOM Correlate software. A minimum of three dog bone specimens were tested for each mixture to ensure reliable results.

As shown in Fig. 7, uniaxial compression tests were performed on ACCCs specimen using a UNITRONIC machine under displacement control at a rate of 0.01 mm/s. Deformation was monitored across the entire specimen area using DIC. The displacement of the specimens was measured using LVDTs. Similarly, the specimens used for DIC measurements were painted white and sprayed with a black speckle pattern. Images were captured every 10 s and processed using GOM Correlate software. The compressive stress-strain curve was obtained by calculating stress as the compressive force divided by the initial cross-sectional area (63 mm × 20 mm) and strain as the applied displacement divided by the initial length (63 mm). Plastic films were used to reduce friction between the specimens and loading plates, facilitating the section rotation to achieve auxetic behavior.

To evaluate the deformation resilience of ACCCs, a sinusoidal cyclic test was conducted to determine the elastic modulus of compressive resilience. The experimental setup with the UNITRONIC machine and the loading plan are shown in Fig. 8. An extended loading plate (Fig. 8a) accommodated horizontal movement during cyclic testing. The specimens were compressed to a displacement of D_{comp} , followed by repeated cycles of compression and release at a frequency of f (Fig. 8b). The test was performed at a frequency (f) of 0.15 Hz (a period T) of 6.67 s) with a 1.0 mm amplitude (A). Based on our previous study [16], D_{comp} was set at 5.0 mm for ACCCs specimen with dimensions in Fig. 4. The stress-strain curve was calculated as in uniaxial compression. At least three replicates were tested for each mixture to obtain reliable results.

3. Results and discussion

3.1. Material properties

Fig. 9a, b, and c show the results of the uniaxial tensile tests for the mixtures SS, SHCC-LS, and SHCC-SS, respectively. Fig. 9d presents the

Table 3
Material properties of PVA fibers.

Fiber type	Diameter (μm)	Length (mm)	Tensile strength (GPa)	Young's modulus (GPa)	Density (g/cm ³)	Ultimate strain
PVA (Reference)	15	6	1.6	34	1.28	6.8 %
PVA (RECS15)	40	8	1.6	41	1.3	6.0 %

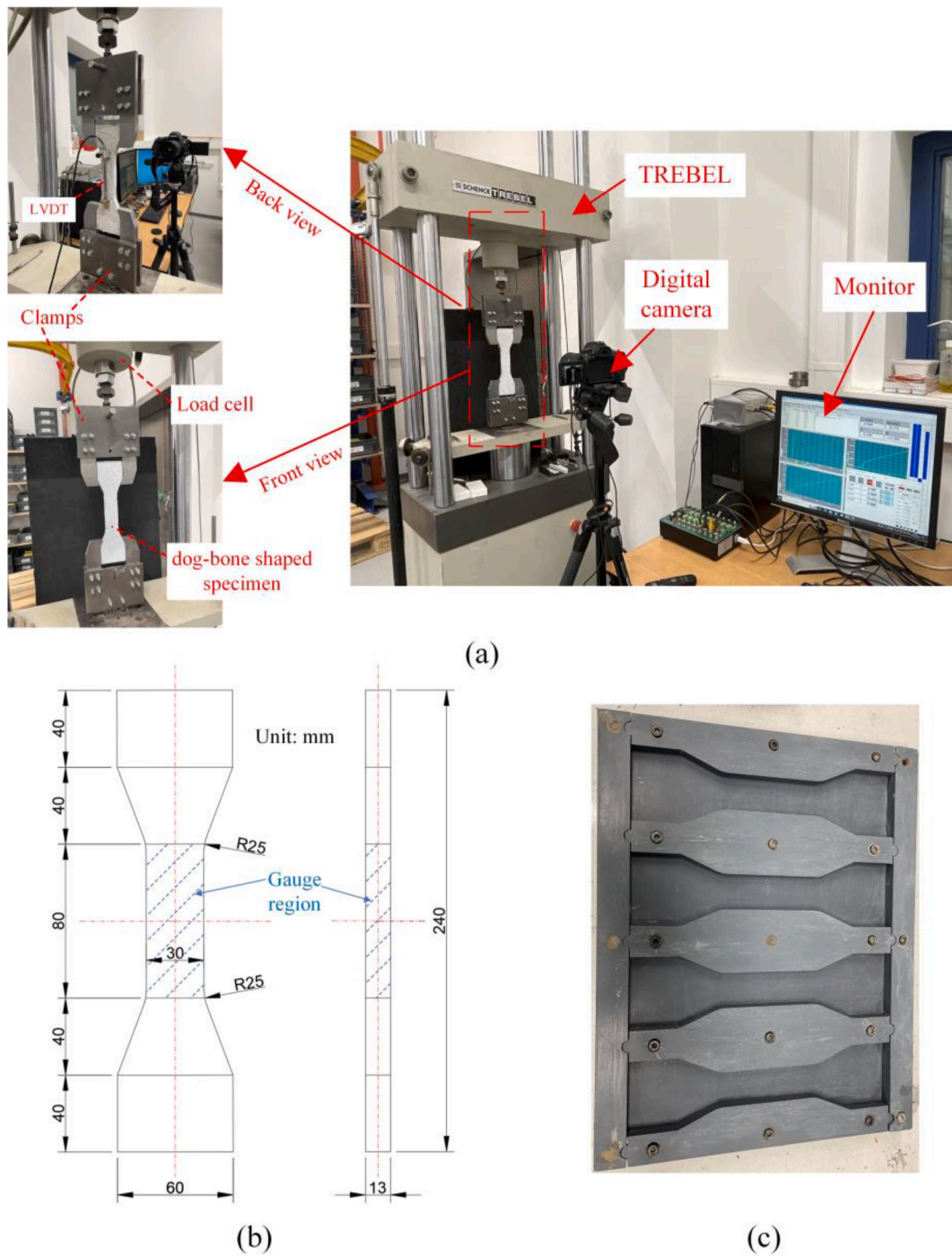


Fig. 6. (a) Setup for uniaxial tensile test using dog bone specimen, (b) dimensions of dog bone specimen, (c) mold for dog bone specimen.

average values of the uniaxial tensile test results for each mixture. The target strain range is selected with a very small interval as the reference strain coordinate for averaging. The experimentally obtained stress curves are then interpolated based on these reference strain coordinates. Finally, the interpolated values at each reference strain coordinate are averaged. To ensure the accuracy of the interpolation results, the spacing of the reference strain coordinates is set significantly smaller than the intervals between the experimental data points. In Fig. 9d, the highest strain point during the strain-hardening process was selected at the strain where the stress exhibits a significant decrease, marking the onset of softening. The starting and ending points of strain-hardening are marked in Fig. 9d, with the strain-hardening starting points

represented by circles within subsets and the ending points shown as solid circles. In this context, the blue color represents SS, the green color indicates SHCC-LS, and the red color signifies SHCC-SS. Table 4 gives detailed tensile properties of the three mixtures. Both SHCC-LS and SHCC-SS displayed tensile strain-hardening behavior, characterized by the emergence of multiple cracks. SHCC-LS demonstrated a moderate tensile strain capacity with strain-hardening behavior observed up to 2.030 % strain, while SHCC-SS exhibited significant strain-hardening behavior extending up to 5.389 % strain due to additional fiber-bridging cracks, as shown in Figs. 9 and 10 and Table 4. Compared to SS, the SHCC mixtures exhibit lower initial cracking strength under tensile loading but higher overall tensile strength, as shown in Figs. 9

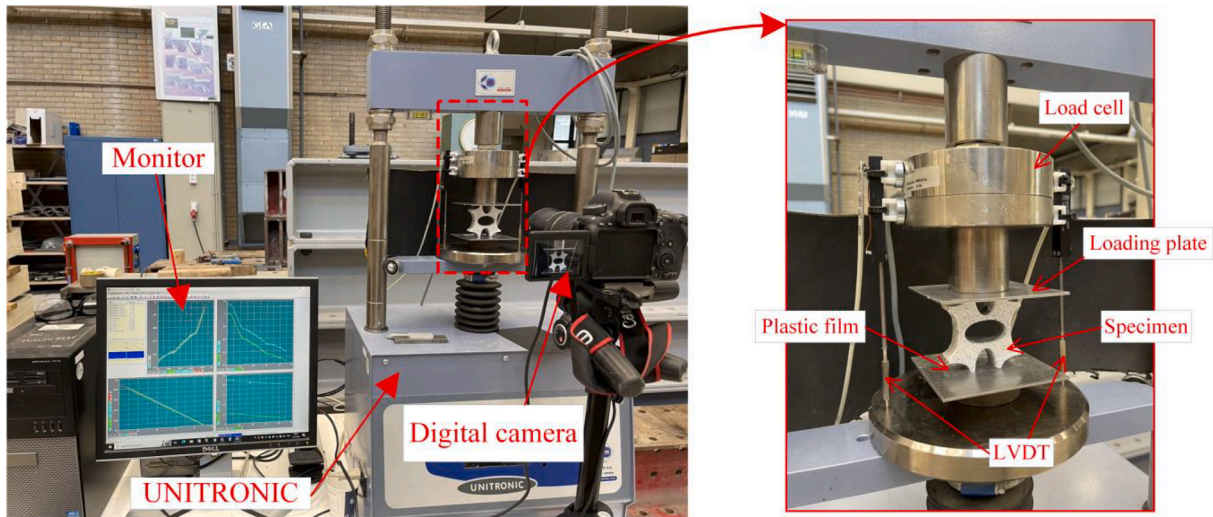


Fig. 7. Experimental setup for uniaxial compression testing of ACCCs.

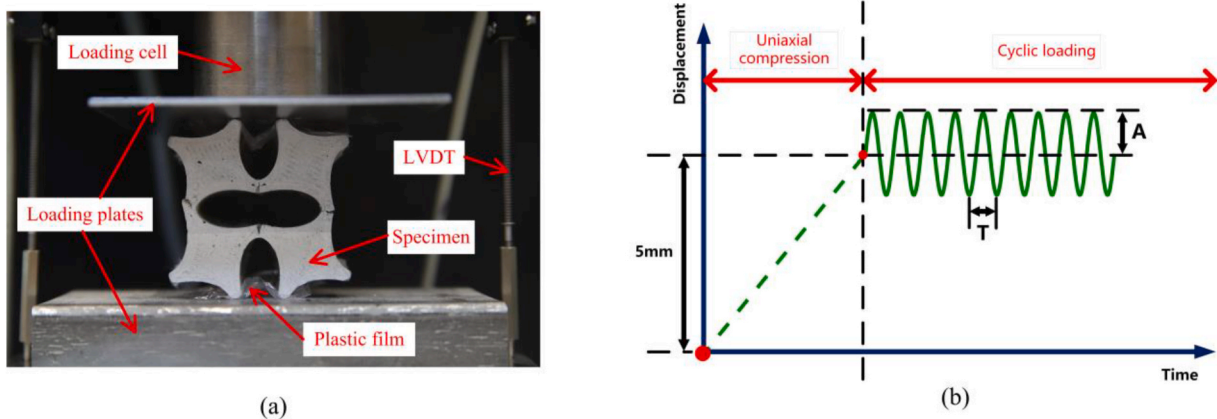


Fig. 8. Cyclic tests of ACCCs, (a) experimental setup, (b) loading plan.

and 10 and Table 4. Fig. 11 displays the major strain distribution of gauge region in the mixtures with SHCC based on DIC analysis. During uniaxial tension, SHCC-LS developed a significant crack at around 2 % strain. As the tension increased, this crack gradually widened to dissipate energy, assisted by a few smaller cracks that also contributed to energy dissipation. In contrast, SHCC-SS showed more fine cracks to dissipate energy during tension, achieving a higher tensile strain capacity. It should be noted that SHCC-LS forms many small cracks at the localization of its main crack, which is due to fiber pull-out in this region. Figs. 9 and 10 and Table 4 also reveal that SHCC-LS has the highest strain softening range of 3.137 % among the three mixtures. In contrast, SHCC-SS exhibits the lowest strain softening range of 1.157 %, despite having the highest tensile strain capacity. Notably, SS shows a strain softening range of 1.934 % even though it lacks strain-hardening behavior, which explains why ACCCs using this mixture still achieves auxetic behavior with low load-bearing capacity in previous study [15]. As has been demonstrated in Section 2.1, ACCCs exhibit auxetic behavior when subjected to large deformations and tend to develop primary cracks with fiber bridging during the later stages of high auxetic behavior. Consequently, the single crack bridging capacity was evaluated for the three mixtures. As illustrated in Fig. 12, SHCC-SS generates more cracks compared to SHCC-LS to achieve a greater tensile strain capacity. However, on average, the fiber bridging within each crack in SHCC-SS sustains a lower tensile strain than that in SHCC-LS.

ACCCs exhibit auxetic behavior through section rotation, which

depends on the widening of crack openings on the tension side at the joint, while the compression side needs the material to have sufficient compressive strength to prevent failure. At the joint where ACCCs contact the loading plate, compressive forces are primarily transferred, and section rotation reduces the compressed contact area, resulting in increased compressive stress. Additionally, after self-contact of ACCCs, the structure predominantly shifts to compression to maintain its integrity, requiring the material to provide adequate compressive strength to ensure stability. The compressive behavior of the fiber-reinforced cementitious matrix was examined through uniaxial compression tests, following the test setup from our previous study [16]. These tests were conducted using the UNITRONIC machine under deformation control at a displacement rate of 0.01 mm/s. To measure displacement, two LVDTs were attached to opposite sides of each specimen. Six cubic specimens (20 mm × 20 mm × 20 mm) were tested in uniaxial compression for each mixture. The peak compressive stress from the stress-strain curve was used to determine the compressive capacity (i.e., compressive strength) of each mixture. Fig. 13 and Table 4 compare the compressive strength of the three mixtures. SHCC-LS and SHCC-SS show higher compressive strength than SS. Generally, when cubic specimens are subjected to compressive failure, they present diagonal cracks caused by the combination of tensile stress and compressive stress. Once cracks appear, the fiber bridging capability in SHCC mixtures prevents them from further propagation. The external energy applied during compression is distributed through the formation

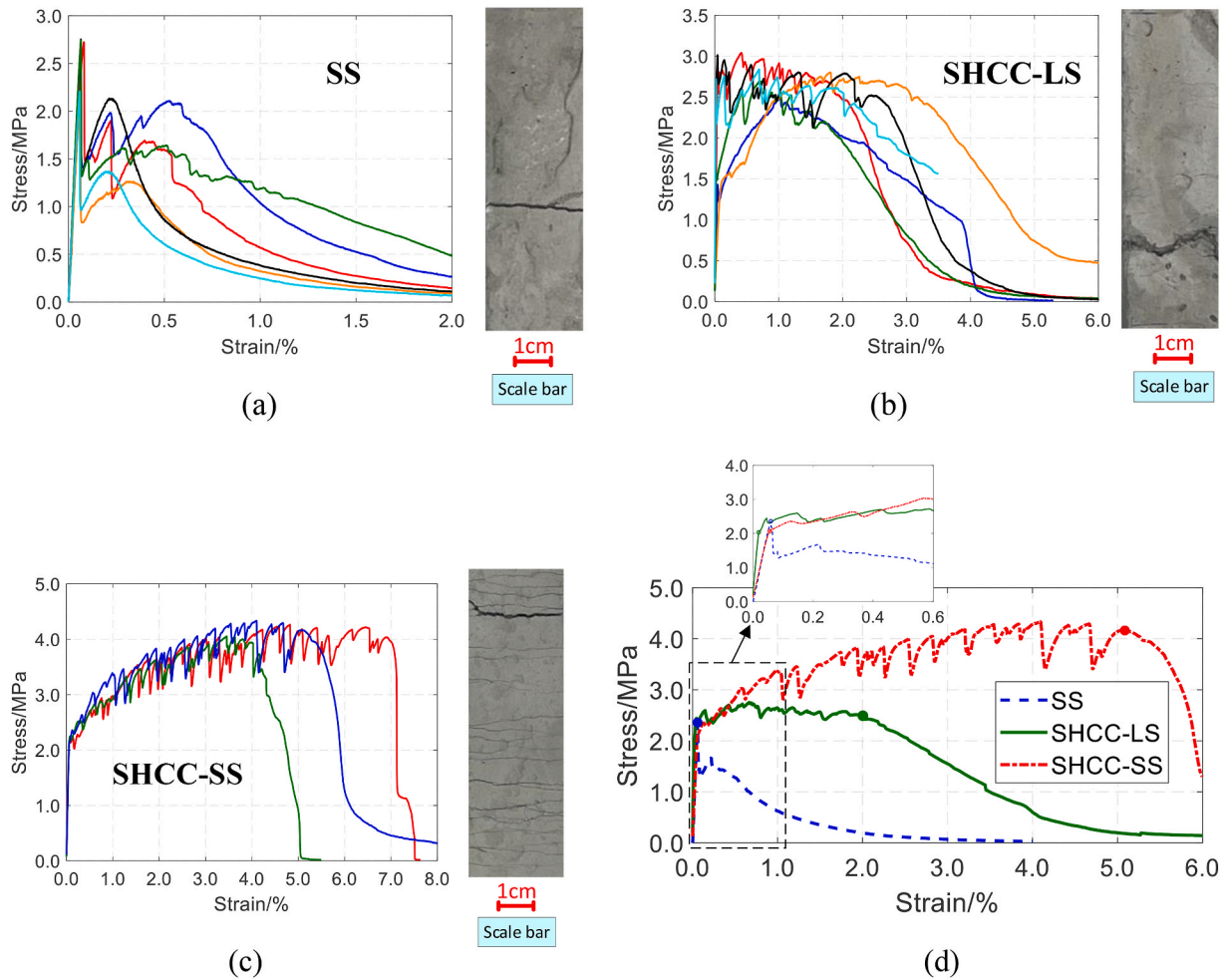


Fig. 9. Uniaxial tensile tests results, (a) SS, (b) SHCC-LS, (c) SHCC-SS, (d) the average values of the three mixtures.

Table 4
Tensile and compressive properties of different mixtures.

Mixture	Tensile properties				Compressive properties
	Initial cracking strength (MPa)	Tensile strength (MPa)	Tensile strain capacity (%)	Strain softening range (%)	Compressive strength (MPa)
SS	2.514 ± 0.129	2.514 ± 0.129	0.066 ± 0.003	1.934 ± 0.003	13.142 ± 0.392
SHCC-LS	2.131 ± 0.291	2.812 ± 0.084	2.030 ± 0.226	3.137 ± 0.154	13.931 ± 0.293
SHCC-SS	2.183 ± 0.035	4.217 ± 0.085	5.389 ± 0.807	1.157 ± 0.391	14.028 ± 0.588

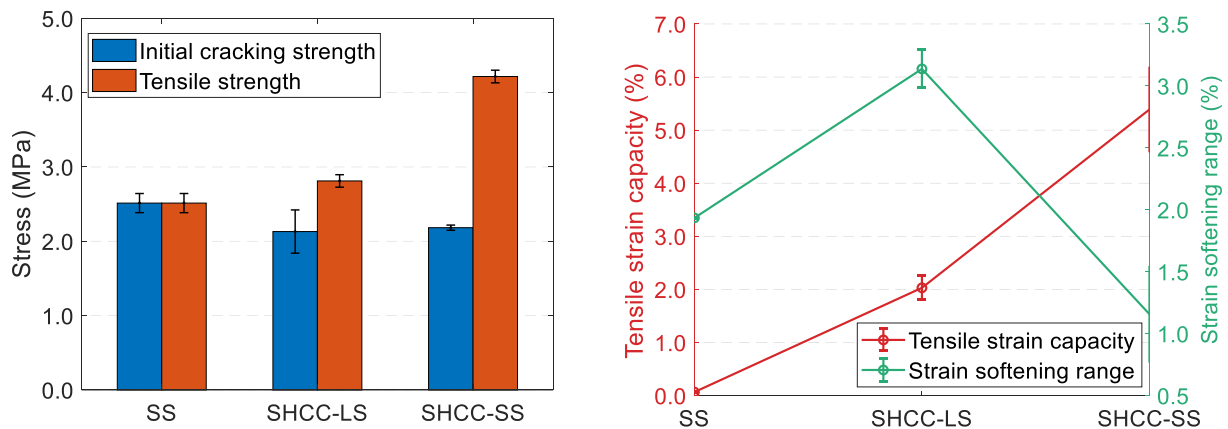


Fig. 10. Comparison of tensile properties of different mixtures (error bars indicate standard deviation).

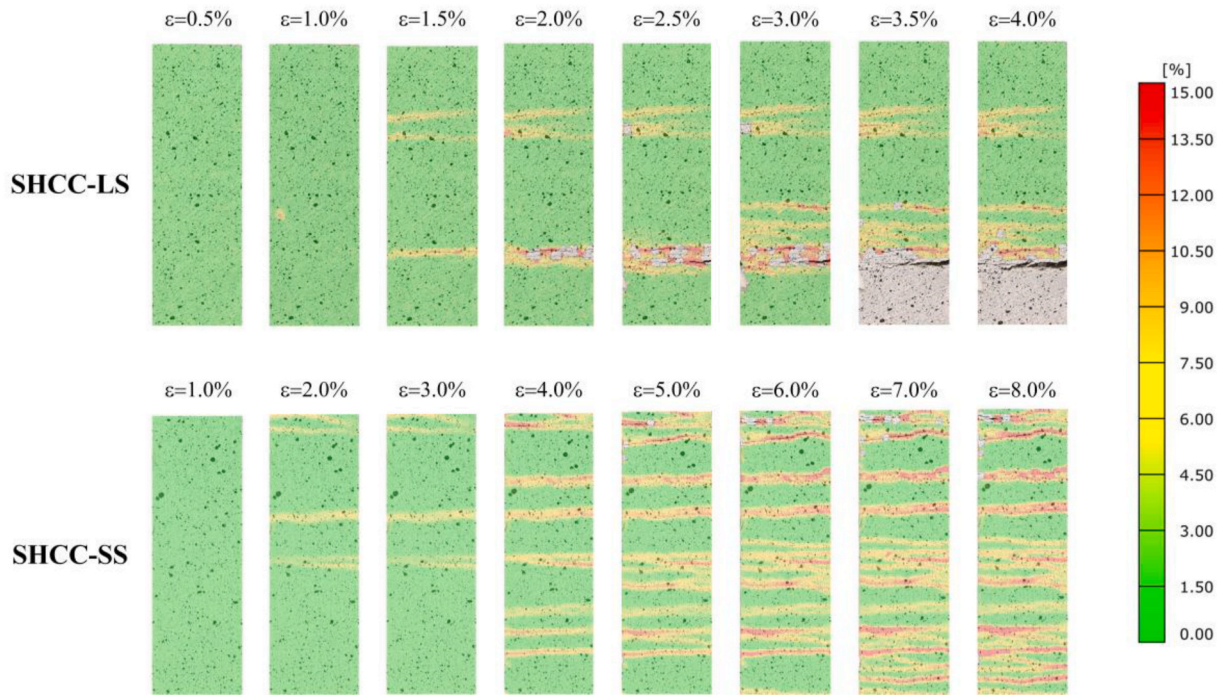


Fig. 11. Major strain distribution during uniaxial tensile tests.

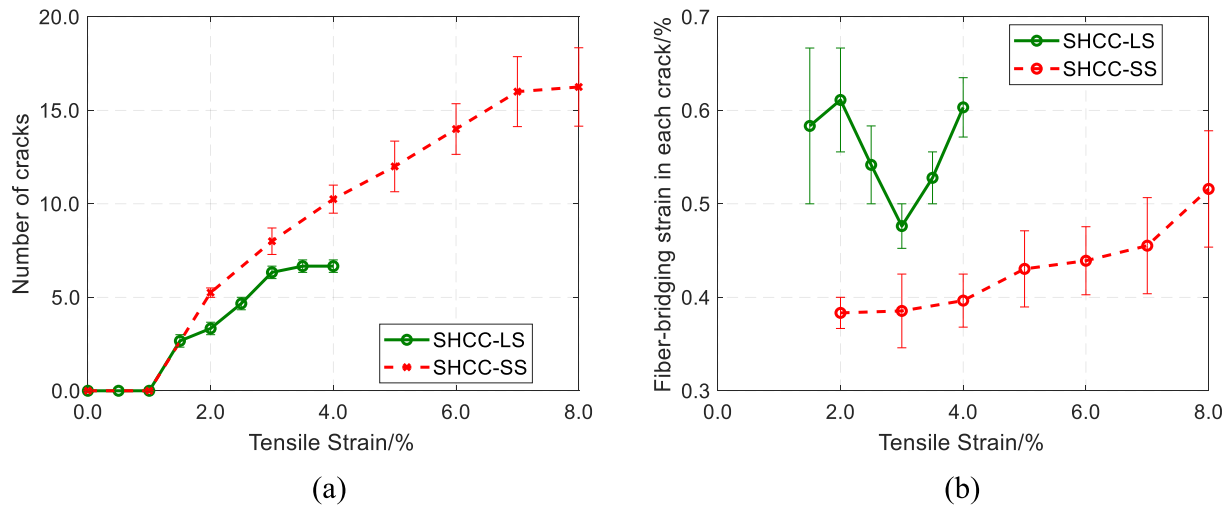


Fig. 12. Tensile properties of the two SHCC mixtures, (a) tensile strain versus number of cracks, (b) tensile strain versus tensile strain sustained by fiber-bridging within each crack (normalized by the gauge length). (Error bars in all plots indicate standard deviation.)

of multiple new cracks, preserving overall structural integrity and enhancing compressive strength.

3.2. Compressive behavior of ACCCs

3.2.1. Compressive stress-strain curve

Fig. 14 compares the stress-strain curves of ACCCs made from the three mixtures under uniaxial compression. The average stress-strain curves of ACCC under uniaxial compression in Fig. 14d were obtained using the same averaging method as in Fig. 9d. The load variation curves of ACCCs using different mixtures under uniaxial compression were given in Appendix B. Fig. 15 illustrates their deformation patterns under uniaxial compression. The mechanical response of ACCCs made from the three mixtures both shows two distinct stages during uniaxial compression, determined by the threshold strain when contact occurs

between the top and bottom ends of the central elliptical-shaped hole (i.e., self-contact within the central elliptical-shaped hole). In Stage I, the initial peak stress of ACCCs made from SHCC mixtures is approximately 0.4 MPa, which is higher than the 0.26 MPa observed in the reference, as seen in Fig. 16 and Table 5. Regarding the range of high auxetic behavior in Stage I, ACCCs made from SHCC mixtures exhibit higher stress compared to the reference. ACCCs made from SHCC-LS exhibit slightly lower stress than SHCC-SS before 6.6 % strain, but slightly higher stress beyond this point. The threshold strains for ACCCs using mixtures of SS, SHCC-LS, and SHCC-SS are 18.67 %, 19.95 %, and 19.37 %, respectively. The reference has the smallest threshold strain, indicating the earliest self-contact or the shortest range of high auxetic behavior due to the largest crack in the joints. Conversely, ACCCs using SHCC mixtures have greater crack resistance capability, delaying the occurrence of self-contact in ACCCs and extending the range of high auxetic behavior.

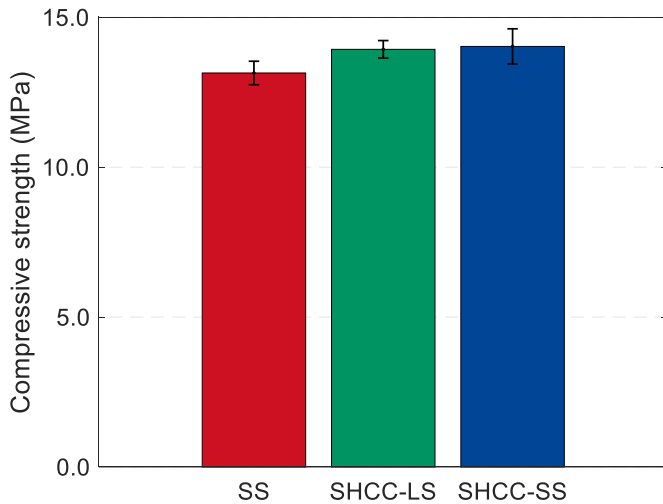


Fig. 13. Compressive strength of different mixtures (error bars indicate standard deviation).

When compared to the SHCC-SS mixture, ACCCs made from SHCC-LS exhibit a higher threshold strain and a more delayed self-contact, indicating a longer range of high auxetic behavior. In Stage II, ACCCs made

from SHCC-SS exhibit a rapid stress increase after self-contact and reach a higher stress level than the other two mixtures. Due to the delayed self-contact, ACCCs made from SHCC-LS show a slower stress increase in Stage II but eventually reach a higher second peak stress than the reference. The second peak stresses of ACCCs made from SHCC-LS and SHCC-SS are 6.00 MPa and 6.42 MPa, respectively, both exceeding the reference's peak stress of 5.03 MPa (see Fig. 16 and Table 5). This indicates that ACCCs using SHCC exhibit enhanced crack resistance and better maintain structural integrity compared to the reference.

3.2.2. Cracking behavior in the hinge joints

The auxetic behavior of ACCCs is due to section rotation and inward folding at the post-cracking hinge joint. The cracking behavior of the hinge joint in the three mixtures were further analyzed, focusing on crack number, the maximum crack mouth opening, and local strain. The maximum crack mouth opening represents the largest crack mouth opening among all cracks in the region, including the largest crack mouth opening formed by the merging of multiple cracks in the later stages of compression. The local strain in the joints is quantified as the ratio of the maximum crack mouth opening to the minor axis length. Using DIC analysis, the maximum crack mouth opening and the number of cracks in the joints were measured at each 5 % increment of compressive strain. As shown in Fig. 17, the number of cracks indicated by high major strain increased rapidly during this initial phase. Hence, the number of cracks was measured at every 1 % increment of

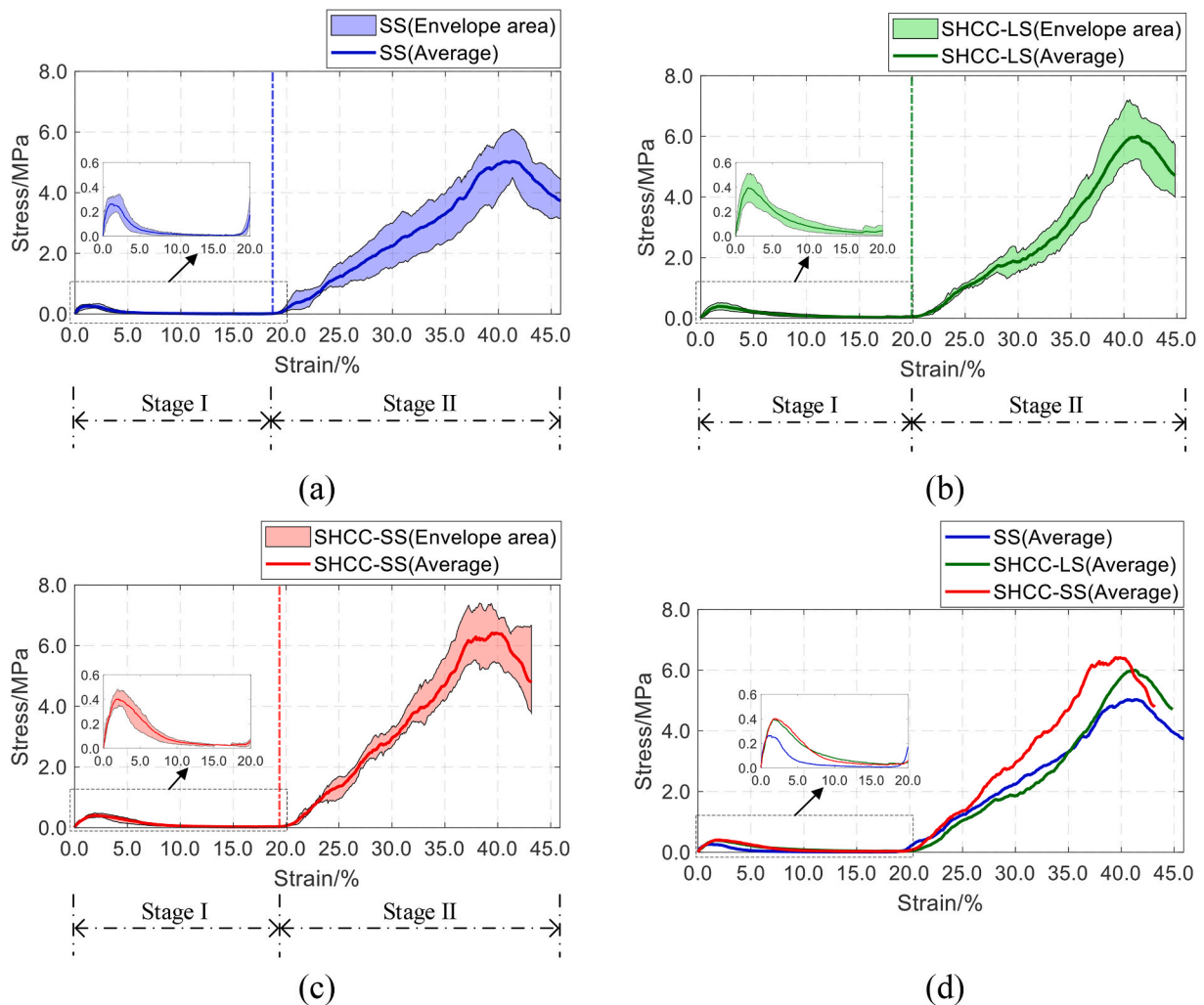


Fig. 14. Stress-strain curve of ACCCs under uniaxial compression, (a) ACCCs using SS, (b) ACCCs using SHCC-LS, (c) ACCCs using SHCC-SS, (d) comparison of the three mixtures.

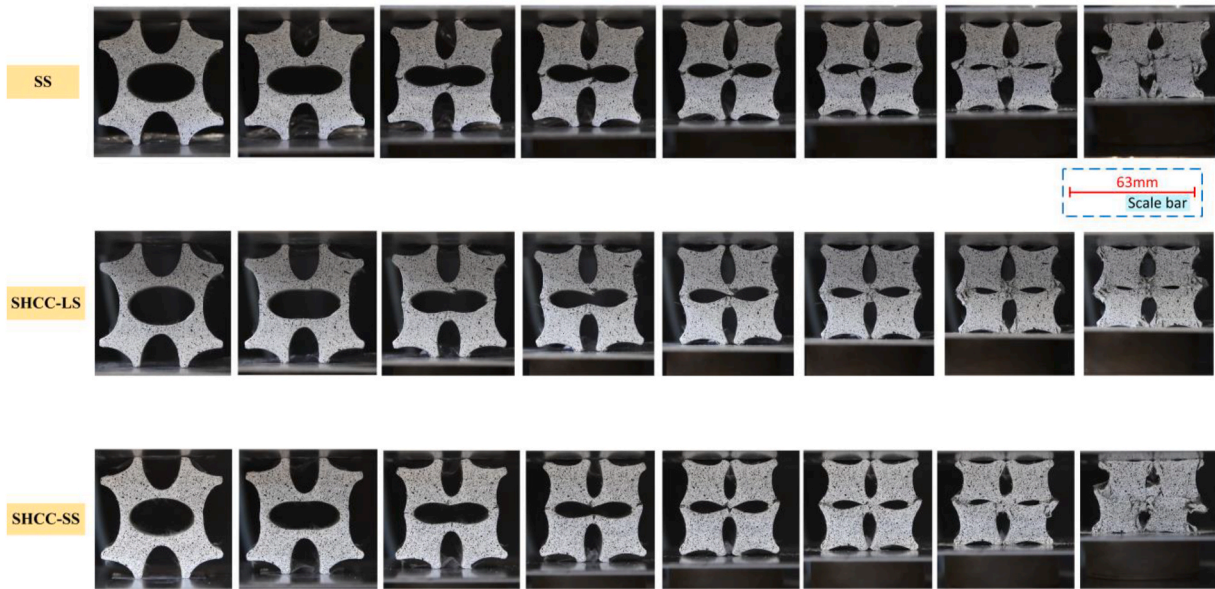


Fig. 15. Deformation of elliptical ACCCs under uniaxial compression for the three mixtures.

Table 5
Comparison of the first peak stress and the second peak stress.

Mixture	First peak stress	Second peak stress
SS	0.263 ± 0.043	5.031 ± 0.469
SHCC-LS	0.394 ± 0.068	6.004 ± 0.568
SHCC-SS	0.402 ± 0.038	6.417 ± 0.539

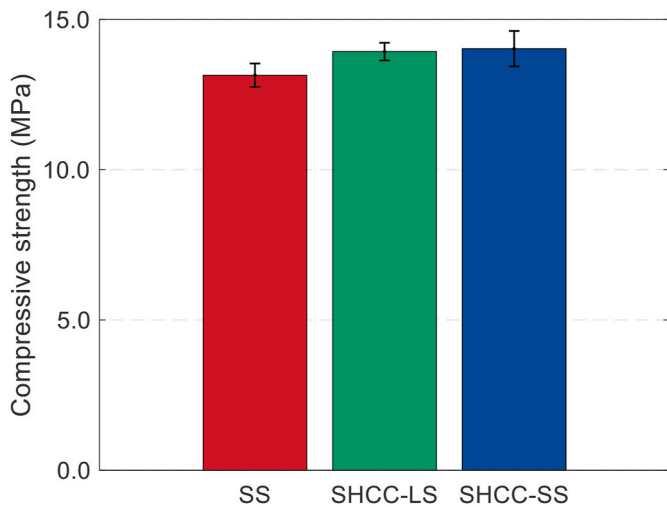


Fig. 16. Comparison of a) the first peak stress, (b) the second peak stress. (Error bars in all plots indicate standard deviation.)

compressive strain up to 5%. The auxetic behavior of ACCCs is triggered by the rotation of sections around the four joints, each functioning as a hinge joint with a certain rotation stiffness. Considering symmetric deformation under uniaxial compression, the average values of these parameters for the top and bottom joints were calculated and are presented in Fig. 18. The number of cracks in the joints increases with rising compressive strain for all three mixtures. ACCCs made from SS have significantly fewer cracks compared to those made from SHCC mixtures. Before 1% strain, ACCCs made from SHCC-SS exhibit slightly more cracks than those made from SHCC-LS due to its greater strain hardening by multiple cracking. Afterwards, ACCCs made from SHCC-LS tend to

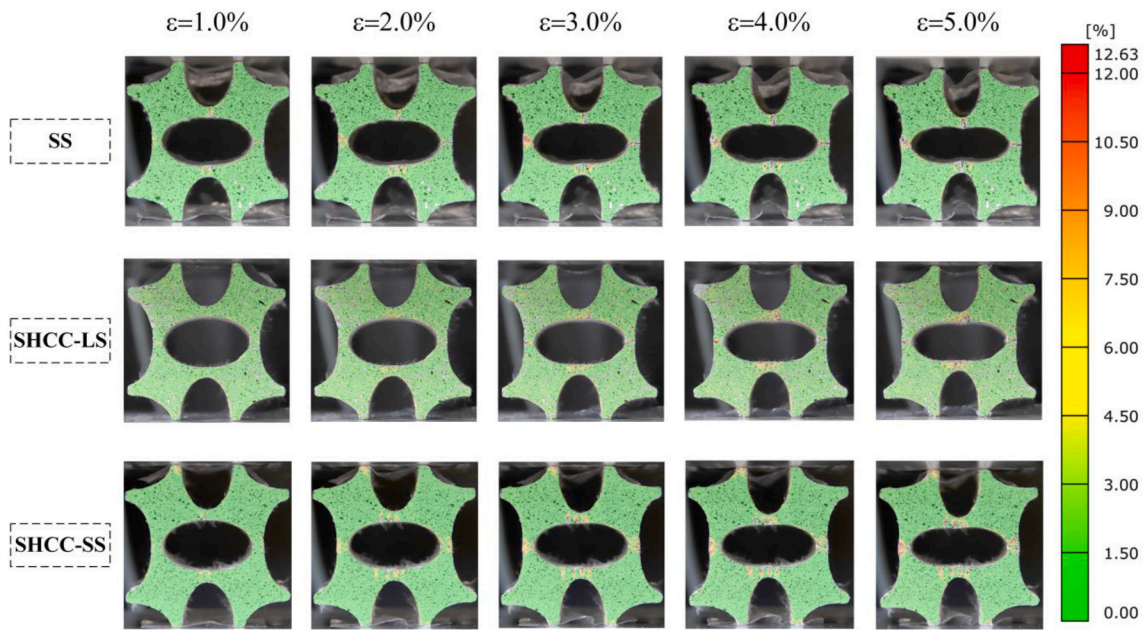
develop more cracks in the joints than those made from SHCC-SS due to fiber pull-out behavior in localized regions. The maximum crack mouth opening in the joints also increases with compressive strain for all three mixtures. ACCCs made from SS have a notably larger maximum crack mouth opening compared to the SHCC mixtures. For ACCCs made from SHCC-LS, the maximum crack mouth opening is slightly lower than those made from SHCC-SS before 5% strain and becomes significantly lower after 5%.

Fig. 19 shows the average values of number of cracks, maximum crack mouth opening, and local strain from the left and right joints. Similarly, for all three mixtures, these parameters from the left and right joints follow the same trend as those from the top and bottom joints. Compared to the top and bottom joints, the left and right joints present fewer cracks for rotation. Because the load transfer direction in the left and right joints aligns with the structure's uniaxial compression, the transferred compressive force reduces the edge tensile stress from bending in these joints. This results in a smaller tensile region and fewer cracks. In contrast, the tensile forces at the top and bottom joints increase the edge tensile stress from bending, expanding the tensile region and leading to more cracks. Hence, the tensile stress at the top and bottom joints in SS quickly reaches yield stress and transitions into the plastic stage. Therefore, there is a significant decrease in load capacity, followed by the initiation and growth of cracks. Conversely, cracks in the left and right joints develop more slowly than those in the top and bottom joints. Further details on the quantitative mechanical analysis of the joints can be found in Appendix C. In SS, tensile stress is mainly managed by a single crack, which accommodates structural rotation and results in a significantly larger maximum crack mouth opening and local strain at the top and bottom joints compared to the left and right joints. In SHCC-based ACCCs, multiple cracks form to distribute the deformation required for structural rotation. This results in similar maximum crack mouth openings and local strain between the top, bottom joints and the left, right joints.

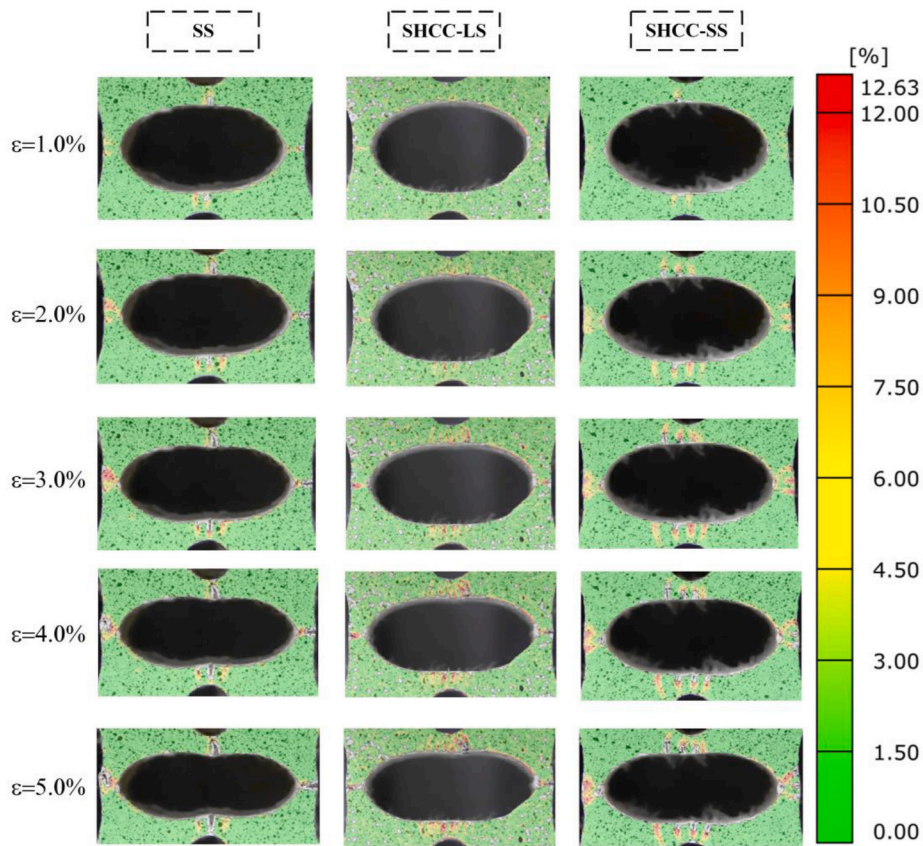
3.2.3. Poisson's ratio variation

$$v = -\frac{\epsilon_x}{\epsilon_y} \tag{1}$$

Based on the DIC analysis, the Poisson's ratio of ACCCs during compression was calculated using the ratio of lateral strain to compressive strain, as described in Eq. (1). Herein, ϵ_x represents the



(a) The entire structure



(b) Crack pattern at the joints.

Fig. 17. Major strain distribution through DIC analysis.

ratio of the maximum projected length ($l_{y,max}$ in Fig. 20a) in the lateral direction (i.e., x-direction) to the initial length in the lateral direction, and ϵ_y denotes the compressive strain (i.e., y-direction).

As shown in Fig. 3, the auxetic behavior in ACCCs under compression

originates from the rotational movement of sections, enabled by fiber bridging at the joints of adjacent holes within the cementitious unit cell. Fig. 20 shows the variation in lateral strain, rotation angle, and Poisson's ratio among ACCC specimens across three different mixtures. The strain

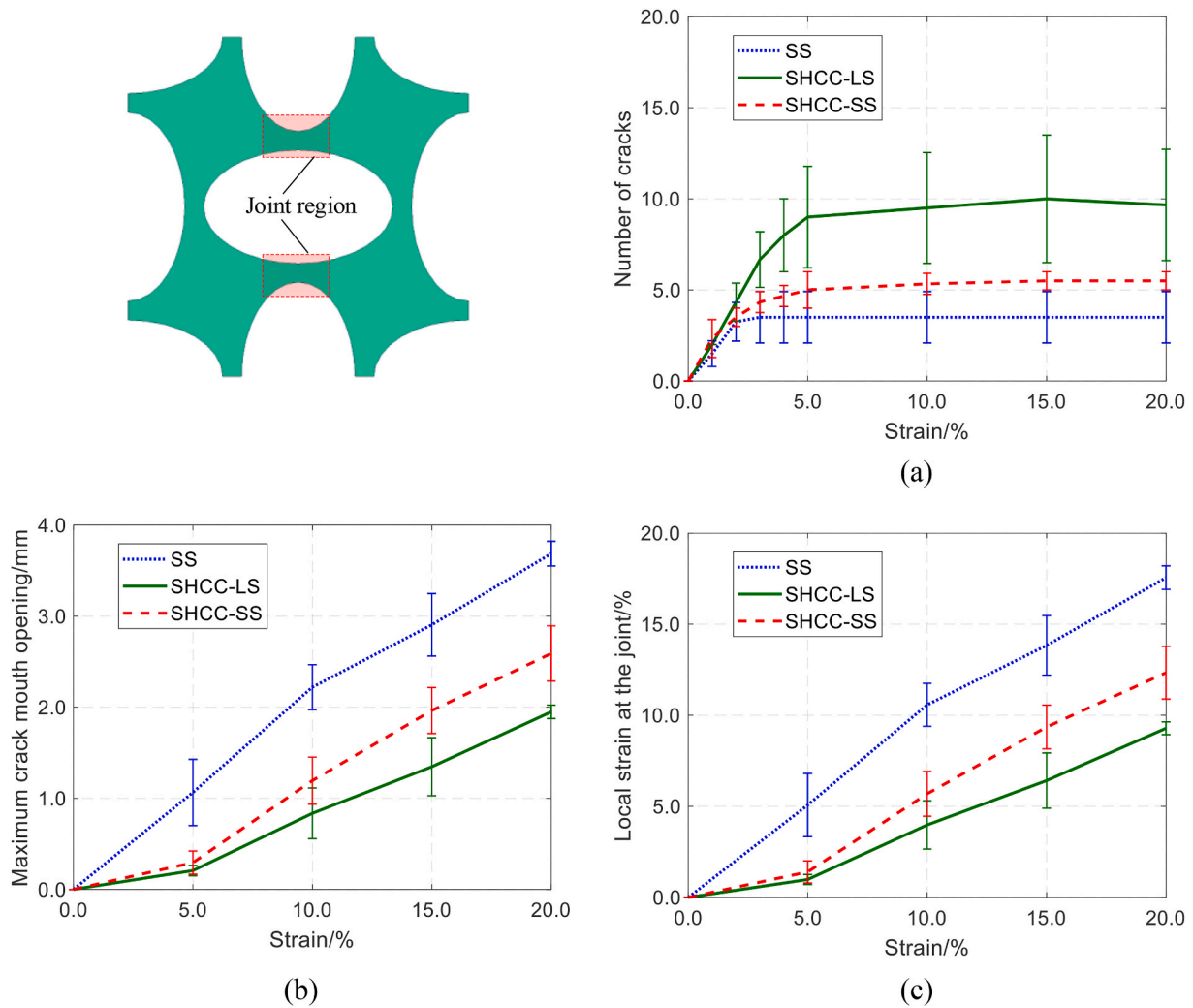


Fig. 18. Number of cracks (a), maximum crack mouth opening (b), local strain (c) in the joints of ACCCs with the three mixtures (top and bottom joints). (Error bars in all plots indicate standard deviation.)

range from 15 % to 20 % is close to self-contact. Therefore, results for an additional 17.5 % strain are included. The rotation angle in Fig. 20c was measured using DIC. In the GOM Correlate software, DIC can determine the angle between two lines—one being the target line and the other serving as the reference axis (i.e., the x-axis or y-axis). As shown in Fig. 20a, the angle θ per frame in DIC is calculated by averaging the angles of each edge at the four end joints (marked as red edges) relative to the y-axis before self-contact occurs. The calculated angle variation during compression is then defined as the rotation angle. As shown in Fig. 20, from 0 % to 15 % strain, as compressive strain increases, all specimens initially exhibit a growing absolute magnitude of a negative Poisson's ratio, characterized by increased lateral contraction during compression due to more pronounced section rotation. Between 15 % and 20 % strain, the absolute value of Poisson's ratio continues to increase for ACCCs with SHCC-SS, whereas for the reference and ACCCs with SHCC-LS, it begins to decrease. This may be because ACCCs with SHCC-SS have the smallest absolute Poisson's ratio among the three, allowing it to continue increasing within this strain range through section rotation. Moreover, this strain range is very close to self-contact. The hinge joint crack is not perfectly centered due to the heterogeneity of the cementitious material, which could lead to the specimen reaching self-contact earlier or causing contact between the end joints (indicated by red edges in Fig. 20a) and the loading plate. These contacts shift the load-bearing mechanism from fiber-bridging in the joints to primarily compression. With its higher compressive strength compared

to SHCC-LS and the reference, SHCC-SS more effectively mitigates contact-induced damage. As a result, the section continues to rotate toward the center, further increasing lateral shrinkage strain in the x-direction and reducing the decline in the absolute value of Poisson's ratio. However, beyond 20 % strain, as self-contact intensifies, the absolute magnitude of the negative Poisson's ratio decreases and begins to transition towards a positive Poisson's ratio. This happens because lateral contraction diminishes when section rotation halts and eventually transitions to lateral expansion under continued compression. The reference shows the shortest duration of a negative Poisson's ratio, with the absolute value of the negative Poisson's ratio rapidly decreasing after self-contact due to its poor crack-resistance capacity and less post-cracking fiber-bridging capacity. Nevertheless, ACCCs with SHCC demonstrate enhanced crack resistance and post-cracking fiber-bridging ability, resulting in a prolonged negative Poisson's ratio that lasts up to 40 %. This accounts for their increased load-bearing capacity observed in the compressive stress-strain curve (Fig. 14) and the maintained structural integrity (Fig. 15). Still, the larger cracks in the reference cause more inward section rotation and greater contraction, leading to a higher absolute value of the negative Poisson's ratio before self-contact. It should be noted that ACCCs with SHCC-LS demonstrate greater lateral contraction, increased section rotation, and a higher absolute magnitude of negative Poisson's ratio before self-contact compared to ACCCs with SHCC-SS. As shown in Figs. 18 and 19, within the high auxetic behavior range, ACCCs with SHCC-LS exhibit a smaller maximum crack mouth

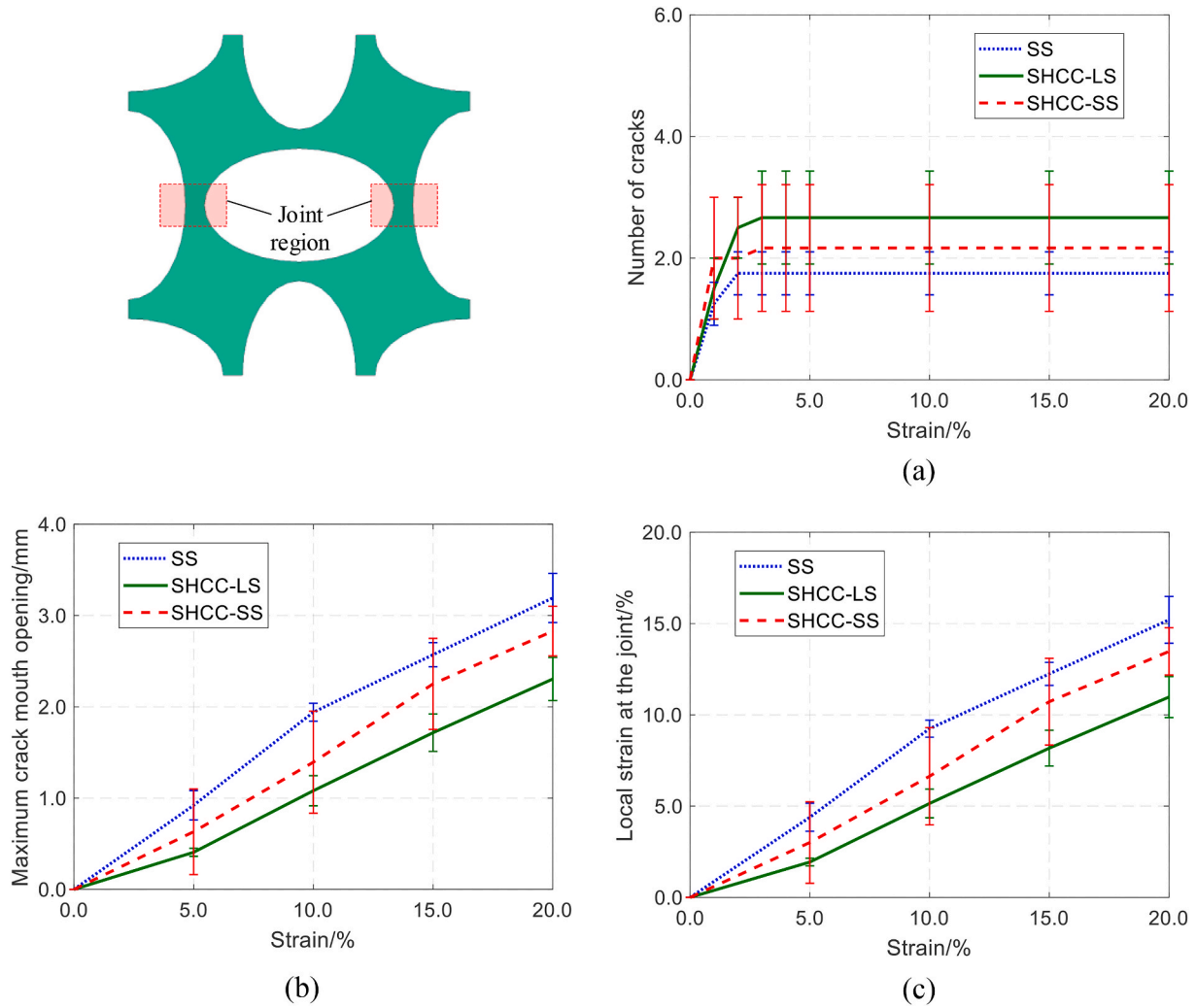


Fig. 19. Number of cracks (a), maximum crack mouth opening (b), local strain (c) in the joints of ACCCs with the three mixtures (left and right joints). (Error bars in all plots indicate standard deviation.)

opening in the joint and a greater number of cracks. This indicates that ACCCs with SHCC-LS accommodate greater deformation by forming more small cracks in the joint, enabling lateral contraction and section rotation while preserving effective fiber bridging and rotational stiffness.

3.2.4. Energy absorption capacity

The specific energy absorption (SEA) per unit volume [16,33,41–43] was calculated using Eq. (2) to remove the influence of material volume on energy absorption during uniaxial compression.

$$SEA = \frac{\int F \cdot dD}{V} = \frac{\int \sigma \cdot d\varepsilon}{\bar{\rho}} \quad (2)$$

where F represents the compressive force, D denotes the vertical displacement, and V stands for the volume of the specimen. The compressive stress σ curve was obtained by calculating stress as the compressive force divided by the initial cross-sectional area (63 mm × 20 mm) and strain ε as the displacement divided by the initial length (63 mm). $\bar{\rho}$ is relative density.

Fig. 21 illustrates the SEA of ACCCs for the three mixtures. All ACCC specimens exhibit a gradual increase in SEA during Stage I, followed by a rapid increase in Stage II. In Stage I, SEA increases slowly due to plastic deformation and crack damage occurring in a limited region at the four joints. After self-contact, in Stage II, ACCCs leverage their entire area to

withstand further compression. This results in continuous plastic deformation and extensive crack damage, leading to a significant rise in SEA. In Stage I, ACCCs from SHCC mixtures exhibit a higher SEA compared to the reference. ACCCs from the SHCC-LS mixture initially have a slightly lower SEA than those from the SHCC-SS mixture up to nearly 12.7 % strain, but then show a slightly higher SEA than the SHCC-SS mixture beyond that point. In Stage II, ACCCs using the SHCC-SS mixture presents a high SEA compared to the other two due to its ductility with multiple cracking and relatively higher tensile and compressive strength. Because of delayed self-contact, ACCCs made from SHCC-LS experience a slower rise in SEA during Stage II but ultimately attain a higher SEA peak than the reference. Fig. 22 and Table 6 compare the SEA of ACCCs using the three different mixtures across various stages. Herein, the accumulated SEA in Stage II was considered only up to the second peak stress in Fig. 14 for each mixture. As shown in Fig. 22a, ACCCs made from SHCC mixtures have a higher accumulated SEA during the entirety of Stage I compared to the reference (SS). By the end of Stage I, ACCCs made from SHCC-LS have a higher SEA of 0.064 J/mm³, compared to 0.058 J/mm³ in ACCCs made from SHCC-SS. In Fig. 22b, the total SEA accumulated during both stages for ACCCs using SS, SHCC-LS, and SHCC-SS mixtures are 1.35 J/mm³, 1.48 J/mm³, and 1.64 J/mm³, respectively. The SEA for ACCCs using SHCC mixtures is higher than the reference, with ACCCs made from SHCC-SS showing a higher SEA than those made from SHCC-LS.

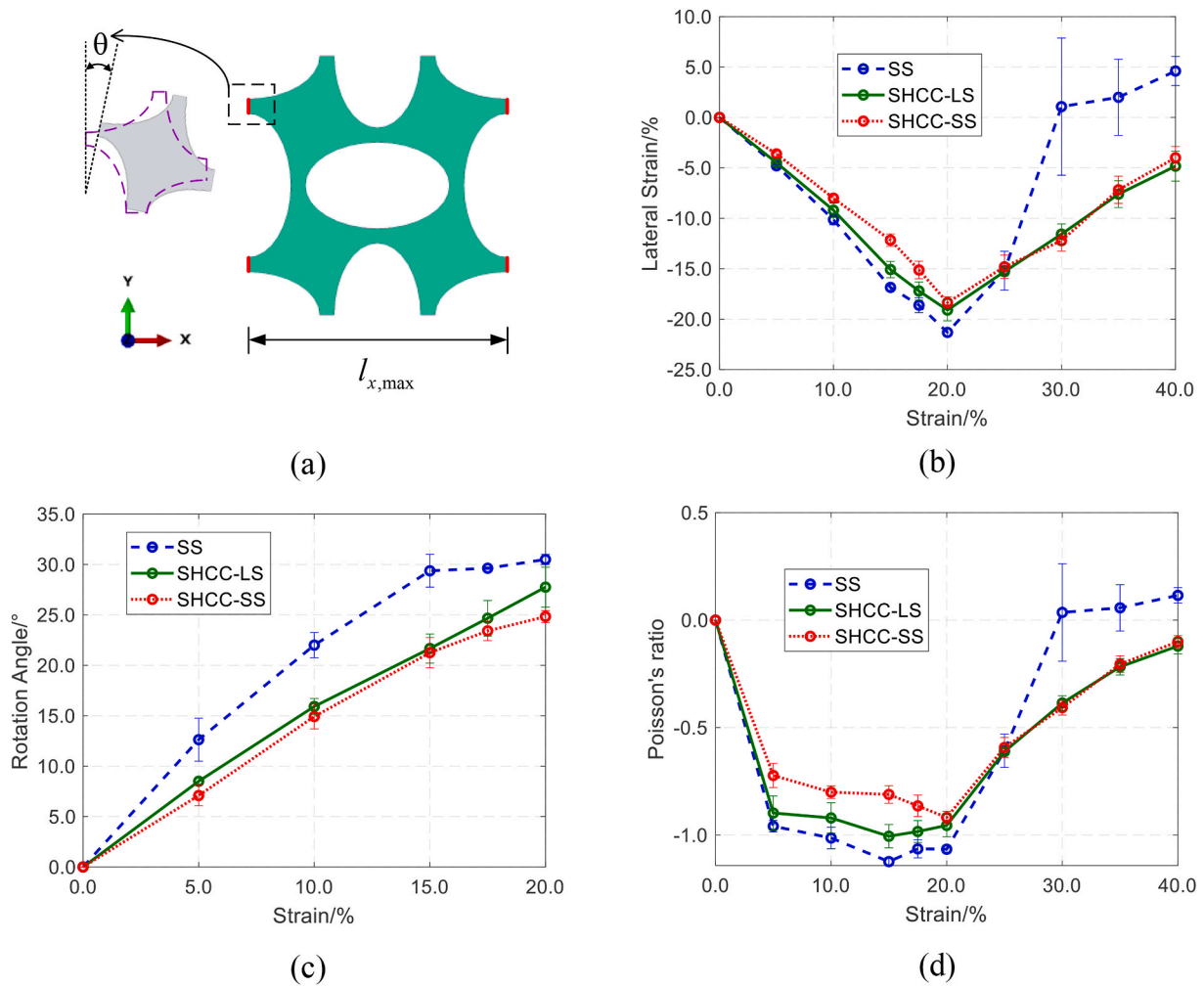


Fig. 20. (a) Schematic diagram of calculations in ACCCs, (b) Lateral strain variation, (c) Rotation angle variation, (d) Poisson's ratio variation. (Error bars in all plots indicate standard deviation.)

3.3. Cyclic test results of ACCCs

Fig. 23 shows the cyclic behavior of ACCCs made from the three mixtures. Three replicates of each mixture were tested under cyclic loading. Fig. 24 and Table 7 present the average response of the three replicates for each mixture. Remarkably, ACCCs demonstrate significant recovery of structural deformation upon the release of compressive loading in cyclic tests, similar to the elastic behavior of elastomers. Despite some plastic deformation or damage, ACCC specimens strive to resume to their original shape when a deforming force is removed — a behavior uncommon in traditional cementitious materials. The terms "compressive deformation resilience" or "recoverable deformation elasticity" are employed to describe the structural recovery or elastic behavior of the entire structure upon the release of compressive stress. In each loading cycle, stress increases concurrently with the rise in compressive displacement. Upon reaching the maximum displacement, the ACCCs specimen reaches peak stress, directly correlating with the applied displacement. Subsequently, as the loading plate gradually moves away from the ACCCs specimen, stress diminishes to nearly negligible levels. Peak-to-peak stress and modulus of elasticity for recoverable deformation for each specimen was calculated by averaging values over ten cycles in Fig. 23. The modulus of elasticity for recoverable deformation was calculated by dividing the peak-to-peak stress by the corresponding strain range. As shown in Fig. 24a, the reference specimen exhibits a lower peak-to-peak stress of 0.0124 ± 0.0004 MPa compared to ACCCs made from SHCC mixtures. ACCCs with the SHCC-

LS mixture have a peak-to-peak stress of 0.0607 ± 0.0033 MPa, higher than the 0.0377 ± 0.0049 MPa observed in ACCCs with the SHCC-SS mixture. Similarly, the reference exhibits a modulus of elasticity for recoverable deformation of 0.3996 ± 0.0004 MPa, as shown in Fig. 24b. Compared to the reference, ACCCs made from SHCC-LS and SHCC-SS achieve elastic moduli of 1.9080 ± 0.1036 MPa and 1.1862 ± 0.1520 MPa, respectively, which are 4.8 and 3.0 times higher. Notably, ACCCs with the SHCC-LS mixture exhibit a greater modulus of elasticity for recoverable deformation than those with the SHCC-SS mixture. Fig. 24c further compares the specific energy absorption of ACCCs per cycle made from the three mixtures. The specific dissipated energy per cycle was determined by calculating the area enclosed between the loading and unloading stress-strain curves for each cycle in Fig. 23, and then dividing this value by the relative density, as indicated in Eq. (2). Herein, these values were averaged over ten cycles in Fig. 23. Among the three mixtures, ACCCs with the SHCC-LS mixture exhibit the highest special energy absorption per cycle at $(6.907 \pm 0.223) \times 10^{-4}$ J, as displayed in Fig. 24c. Herein, ACCCs using the SHCC-SS mixture also show a higher special energy absorption of $(4.550 \pm 0.941) \times 10^{-4}$ J per cycle, compared to $(1.628 \pm 0.366) \times 10^{-4}$ J in the reference mixture. This is attributed to the reference (SS) having significantly lower fiber-bridging capacity, which reduces rotational stiffness in the pseudo-hinge joints. As a result, its peak stress and modulus of elasticity for recoverable deformation are lower than those of SHCC-based ACCCs, leading to decreased energy absorption during cyclic loading. Furthermore, ACCCs exhibit high ductility, with a wide compression

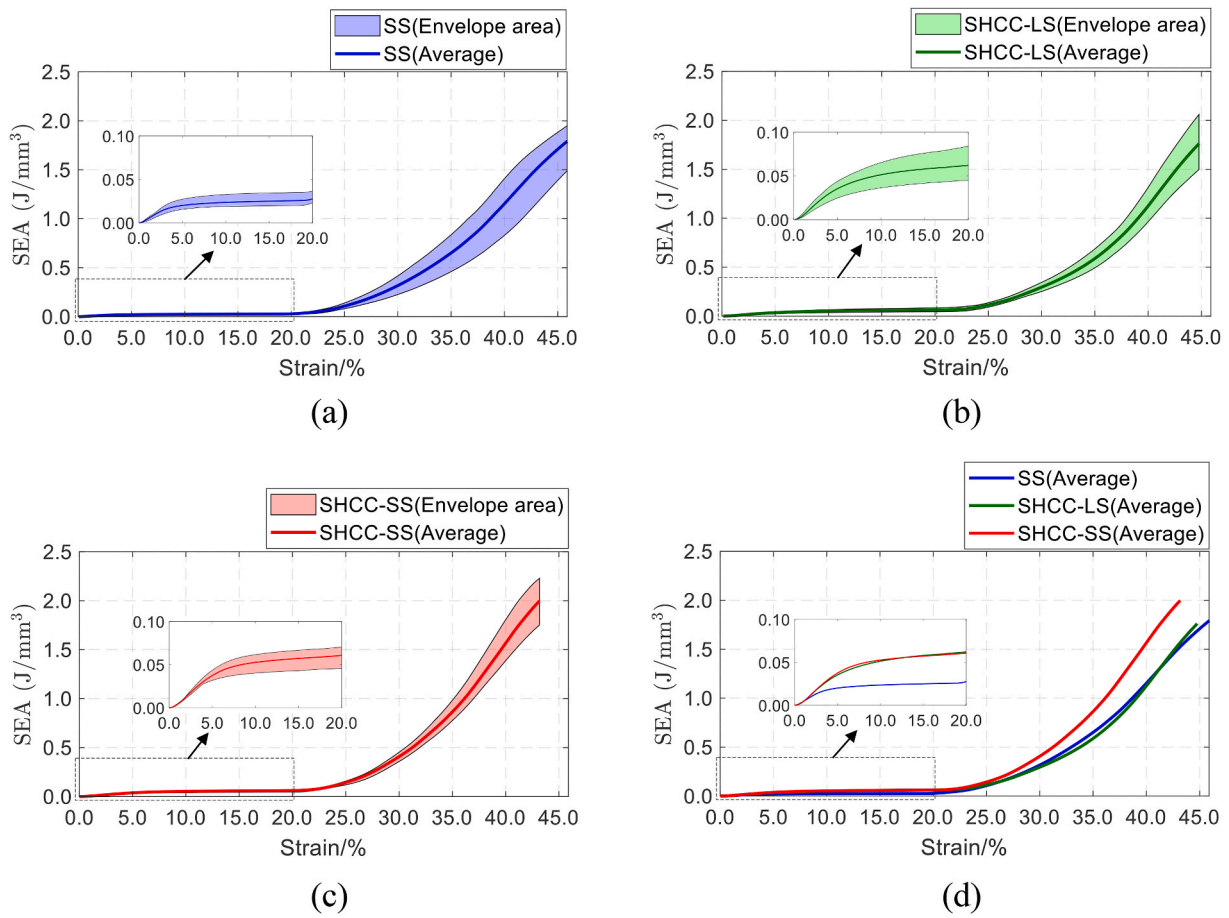


Fig. 21. Specific energy dissipation, (a) ACCCs made from SS, (b) ACCCs made from SHCC-LS, (c) ACCCs made from SHCC-SS, (d) comparison of the three mixtures.

Table 6
Comparison of specific energy absorption of ACCCs with the three mixtures.

Mixture	Stage I (J/mm ³)	Stage I+ Stage II (J/mm ³)
SS	0.027 ± 0.004	1.348 ± 0.173
SHCC-LS	0.064 ± 0.011	1.484 ± 0.132
SHCC-SS	0.058 ± 0.007	1.640 ± 0.125

deformation range from the first peak stress to the point of significant stress drop after the second peak stress under uniaxial compression. This elastomer-like behavior during cyclic loading utilizes ductility within the high auxetic deformation range. Specifically, SHCC-based ACCCs utilize this ductility to sustain greater stiffness for recoverable deformation within a certain range during cyclic loading, thereby improving the energy absorption. SHCC-LS outperforms SHCC-SS in both the energy absorption and ductility due to its higher modulus of elasticity for recoverable deformation, allowing it to achieve greater peak stress. This advantage stems from enhanced fiber bridging in primary cracks

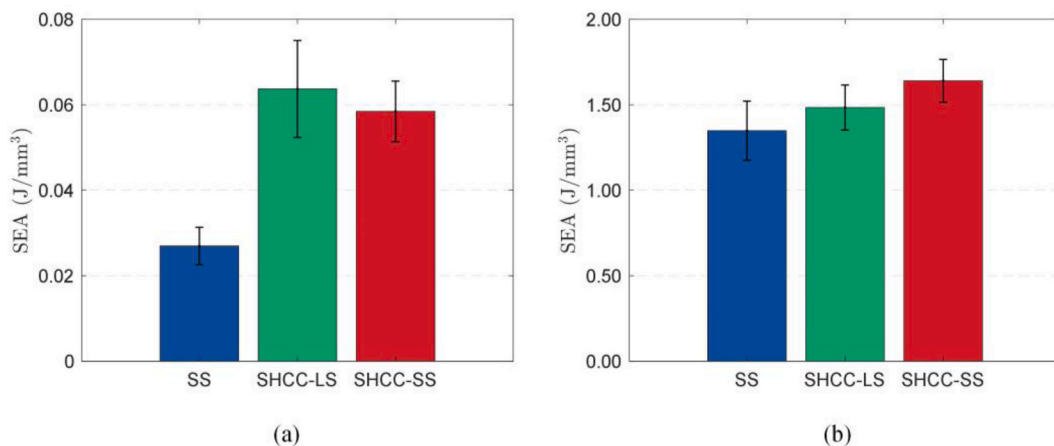


Fig. 22. Comparison of specific energy absorption of ACCCs with the three mixtures, (a) Stage I, (b) Stage I+ Stage II. (Error bars in all plots indicate standard deviation.)

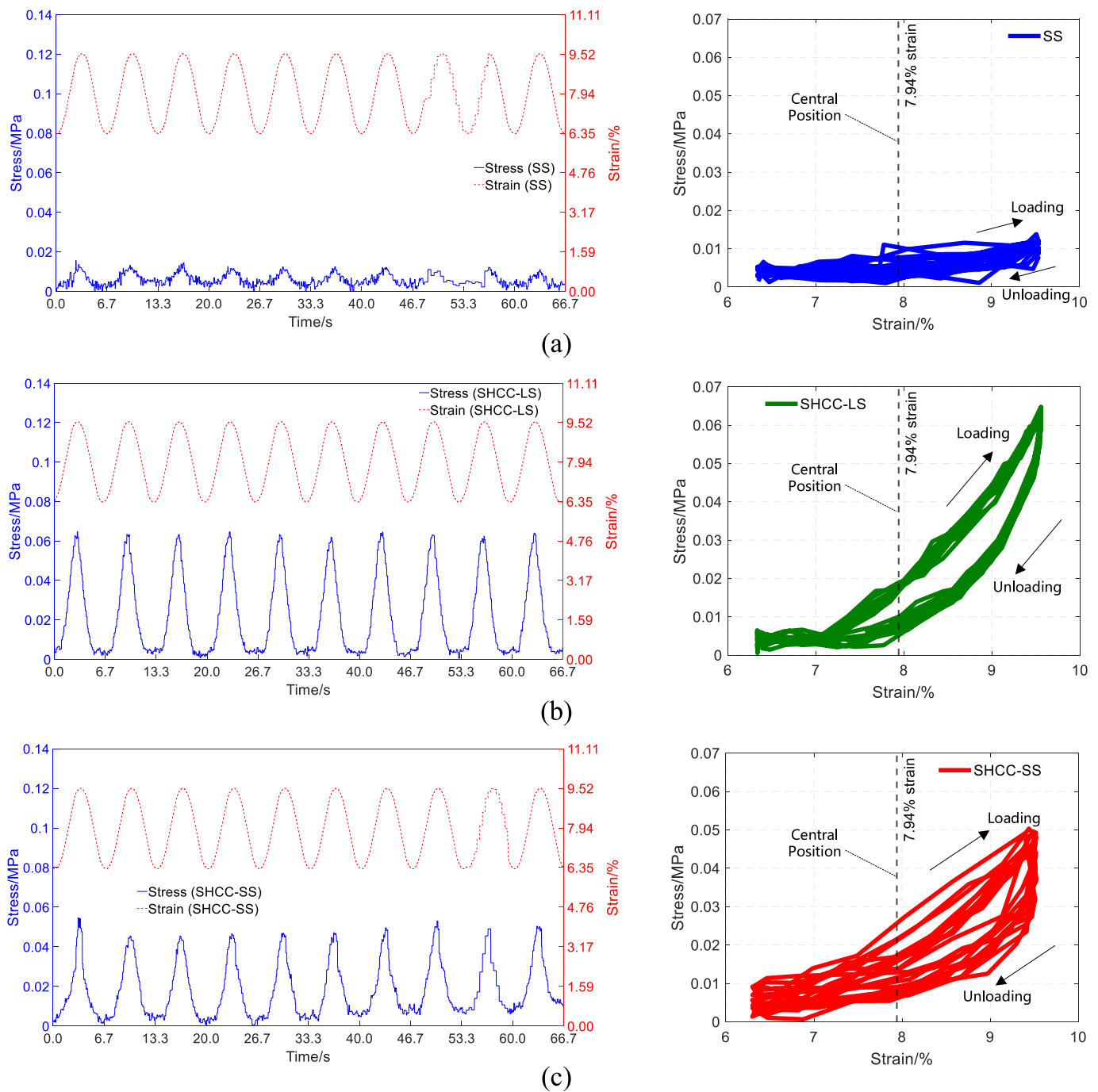


Fig. 23. Cyclic behavior of ACCCs specimens, (a) SS, (b) SHCC-Ls, (b) SHCC-SS.

through extended softening.

The specimens were initially compressed to a displacement of 5.0 mm (7.94 % compressive strain) and then subjected to a cyclic test with repeated compression and release cycles at a frequency of 0.15 Hz. The cyclic test was conducted with an amplitude (A) of 1.0 mm, corresponding to a compressive strain range of 6.35 %–9.52 %. This strain range falls within the region of high auxetic behavior, as described in the Introduction (extending from the first peak stress point to the self-contact point). Fig. 25 depicts the deformation resilience patterns of ACCCs using the three mixtures during each cycle of compression and release. Each red point represents the loading state of the three ACCCs within each sinusoidal cycle. From top to bottom, each row in Fig. 25 represents the deformation resilience pattern of specimens at the trough, central position, and peak of the sinusoidal loading cycle. The stress-

strain curve remains nearly identical across the ten cycles in Fig. 23, and the deformation resilience pattern is nearly consistent. Therefore, deformation images from one of these cycles were selected for comparison. Unlike the single primary crack in the joints of the reference, ACCCs with the SHCC mixtures show a smaller primary crack accompanied by surrounding minor cracks. Fiber bridging in both the primary and minor cracks enhances the rotational stiffness of these ACCCs. After cyclic tests, a digital optical microscope was utilized to study fiber bridging and pull-out behaviors at the cracks in the joints between adjacent holes in ACCCs using the three mixtures (see Appendix D). More details regarding the recoverable deformation of SHCC-based ACCCs can be found in the videos included in the Supplementary data. To further verify the advantages of the material proposed in this study, another cell type of ACCCs (P1-thick) was fabricated and tested (see

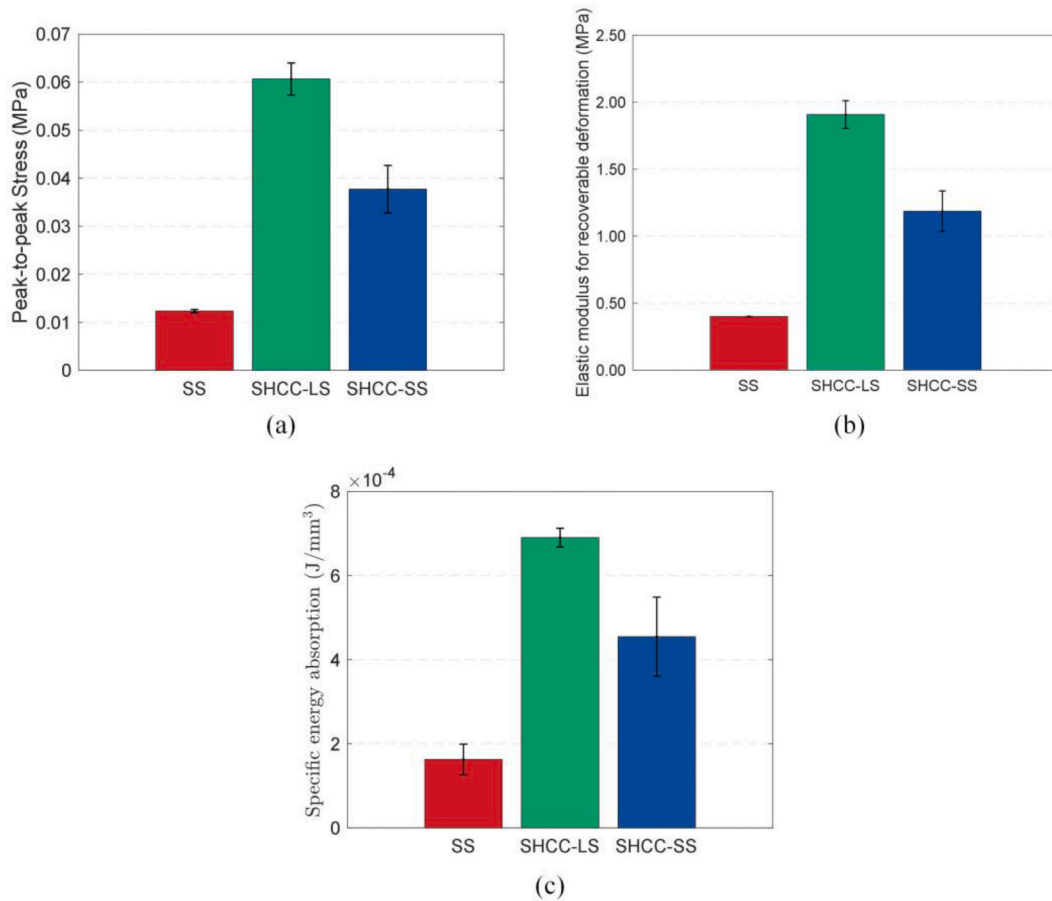


Fig. 24. (a) Peak-to-peak stress during cyclic loading, (b) recoverable deformation elasticity during cyclic loading, (c) specific energy absorption per cycle. (Error bars in all plots indicate standard deviation.)

Table 7
Comparison of cyclic test results of ACCCs with the three mixtures.

Mixture	Peak-to-peak Stress (MPa)	Elastic modulus for recoverable deformation (MPa)	Specific energy absorption (J/mm ³)
SS	0.0124 ± 0.0004	0.3996 ± 0.0004	1.628e-4 ± 0.366e-4
SHCC-LS	0.0607 ± 0.0033	1.9080 ± 0.1036	6.907e-4 ± 0.223e-4
SHCC-SS	0.0377 ± 0.0049	1.1862 ± 0.1520	4.550e-4 ± 0.941e-4

Appendix E), featuring an increased joint thickness based on modifications to the P1-shaped ACCC design.

4. Conclusions

This study created elliptical ACCCs using two SHCC types—shortened softening and prolonged softening—through additive manufacturing-assisted casting. The ACCCs were tested for compressive behavior, compressive strength, Poisson’s ratio, and energy dissipation with DIC. Then, cyclic tests were performed to assess compressive deformation resilience. The test results were compared to a strain-softening fiber-reinforced cementitious reference mixture. The main conclusions can be presented as follows:

(1) Compared to the reference (SS), ACCCs made with SHCC mixtures accommodate greater joint rotation by developing multiple cracks with strain hardening. This postpones the onset of primary

cracks and further reduces the opening of the primary crack. In the later stages, the significant section rotation of ACCCs results in the formation of a primary crack in the joints. Utilizing SHCC with extended softening helps maintain effective fiber bridging within the primary crack and enhance rotational stiffness in the pseudo-hinge joints. As a result, this SHCC mixture enhances load-bearing capacity and recoverable deformation elasticity within the high auxetic behavior range of ACCCs.

- (2) Compared to the reference (SS), ACCCs made from SHCC exhibit superior load-bearing capacity during high auxetic behavior range and stable auxetic behavior under uniaxial compression. Following self-contact, ACCCs made from SHCC mitigate the reduction in the magnitude of the negative Poisson’s ratio due to their crack-resistance capacity and sustain a negative Poisson’s ratio up to a considerably high compressive strain. Their strong fiber-bridging and crack resistance capabilities enhance the structure’s ductility and toughness, preventing splitting failure and preserving structural integrity. As a result, they show higher specific energy absorption than the reference (SS).
- (3) Compared to the reference (SS), P1-shaped ACCCs made from SHCC-LS and SHCC-SS exhibit elastic moduli for recoverable deformation that are 4.8 and 3.0 times higher, respectively. Despite SHCC-LS having lower strain hardening than SHCC-SS, ACCCs made from SHCC-LS demonstrate greater recoverable deformation elasticity due to its extended softening capacity. This extended softening enhances fiber-bridging within the primary crack in the joints of ACCCs, as observed by microstructural analysis.

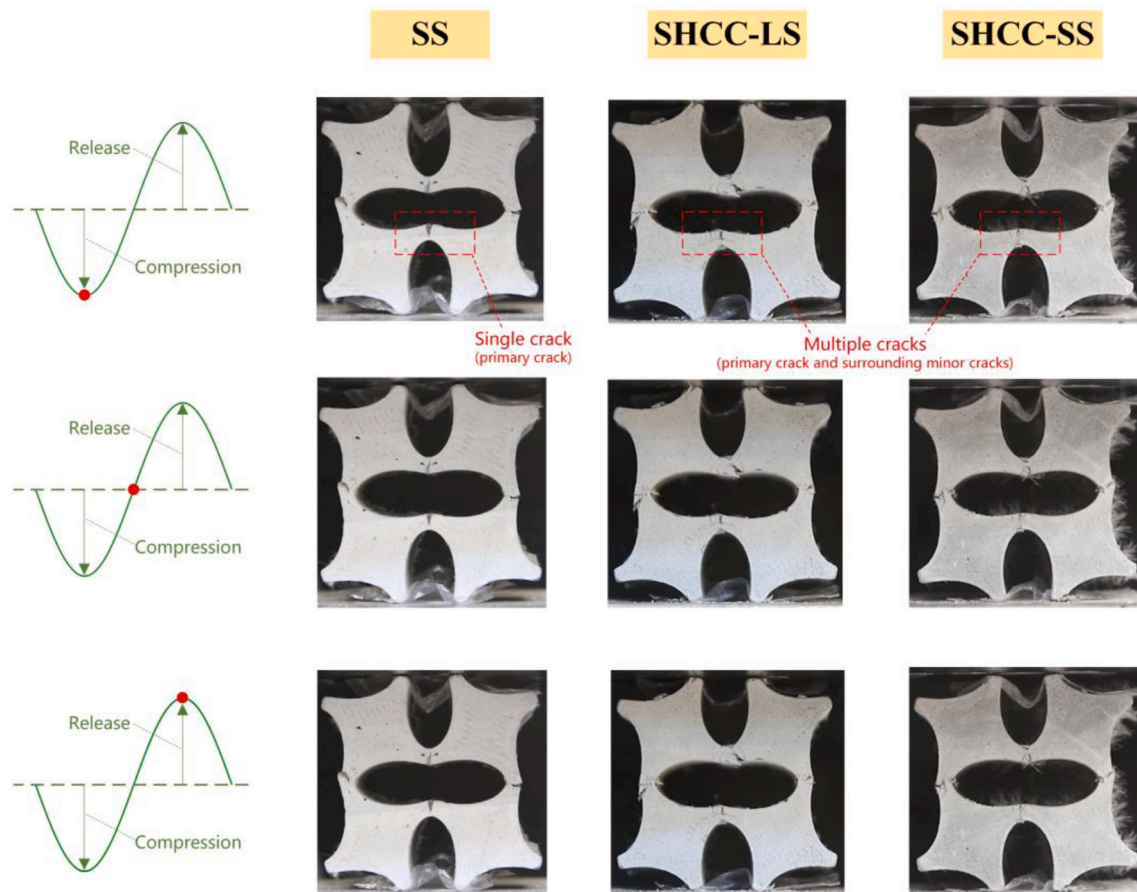


Fig. 25. Deformation resilience pattern of ACCCs with different mixtures.

Using the SHCC mixture with extended softening provides stable auxetic behavior, which is applicable to various ACCCs shapes requiring strong fiber bridging and crack resistance. This broadens the engineering applications of auxetic cementitious elastomers to different load levels and scenarios. Their exceptional mechanical properties allow for effective impact energy absorption in infrastructure applications such as speed humps, seismic isolators, and engineered materials arresting systems (EMAS) for aircraft overrun mitigation [22,44]. Furthermore, their elastomer-like behavior under high auxetic deformation can be leveraged for multifunctional cementitious materials, such as energy harvesters and sensors for smart infrastructure. However, this study is limited to a specific SHCC-LS mixture with an initial strain hardening phase followed by extended softening. Adjusting these phases can further optimize ACCCs' static compression and elastomer-like behavior under cyclic loading. Further research is also needed to investigate the micro-mechanisms of SHCC-LS for microstructural-based design and performance improvement. Future studies should also examine multiple cells of ACCCs to account for the effects of interactions between adjacent cells and the heterogeneity of cementitious materials.

CRedit authorship contribution statement

Jinbao Xie: Writing – review & editing, Writing – original draft, Visualization, Validation, Software, Methodology, Investigation, Formal analysis, Data curation, Conceptualization. **Shan He:** Writing – review & editing, Methodology, Investigation, Formal analysis, Conceptualization. **Yading Xu:** Writing – review & editing, Software, Methodology. **Zhaozheng Meng:** Writing – review & editing, Visualization,

Investigation. **Wen Zhou:** Writing – review & editing, Validation, Methodology. **Erik Schlangen:** Writing – review & editing, Validation, Supervision, Resources, Methodology. **Branko Šavija:** Writing – review & editing, Validation, Supervision, Resources, Project administration, Methodology, Funding acquisition, Conceptualization.

Declaration of competing interest

The authors declare that they have no known competing financial interests or personal relationships that could have appeared to influence the work reported in this paper.

Acknowledgements

Jinbao Xie would like to acknowledge the funding supported by China Scholarship Council (CSC) under the grant CSC No. 202006260045. The experimental part of the study was funded by the Dutch Research Council (NWO) through the Open Mind Project “Auxetic Concrete Energy Harvester”, grant number 18764. Yading Xu, Zhaozheng Meng, Wen Zhou and Branko Šavija acknowledge the financial support of the European Research Council (ERC) within the framework of the ERC Starting Grant Project “Auxetic Cementitious Composites by 3D printing (ACC-3D)”, Grant Agreement Number 101041342. Views and opinions expressed are however those of the author(s) only and do not necessarily reflect those of the European Union or the European Research Council. Neither the European Union nor the granting authority can be held responsible for them.

Appendix A. Ingredients used for mixture designs



CEM I 42.5 N



Fly ash



Sand
(grain size 125~250 μm)



VMA



PVA (AC-R)



PVA (RECS15)

Fig. A1. Ingredients used for mixture designs

Appendix B. Load variation curve of ACCCs using different mixtures under uniaxial compression

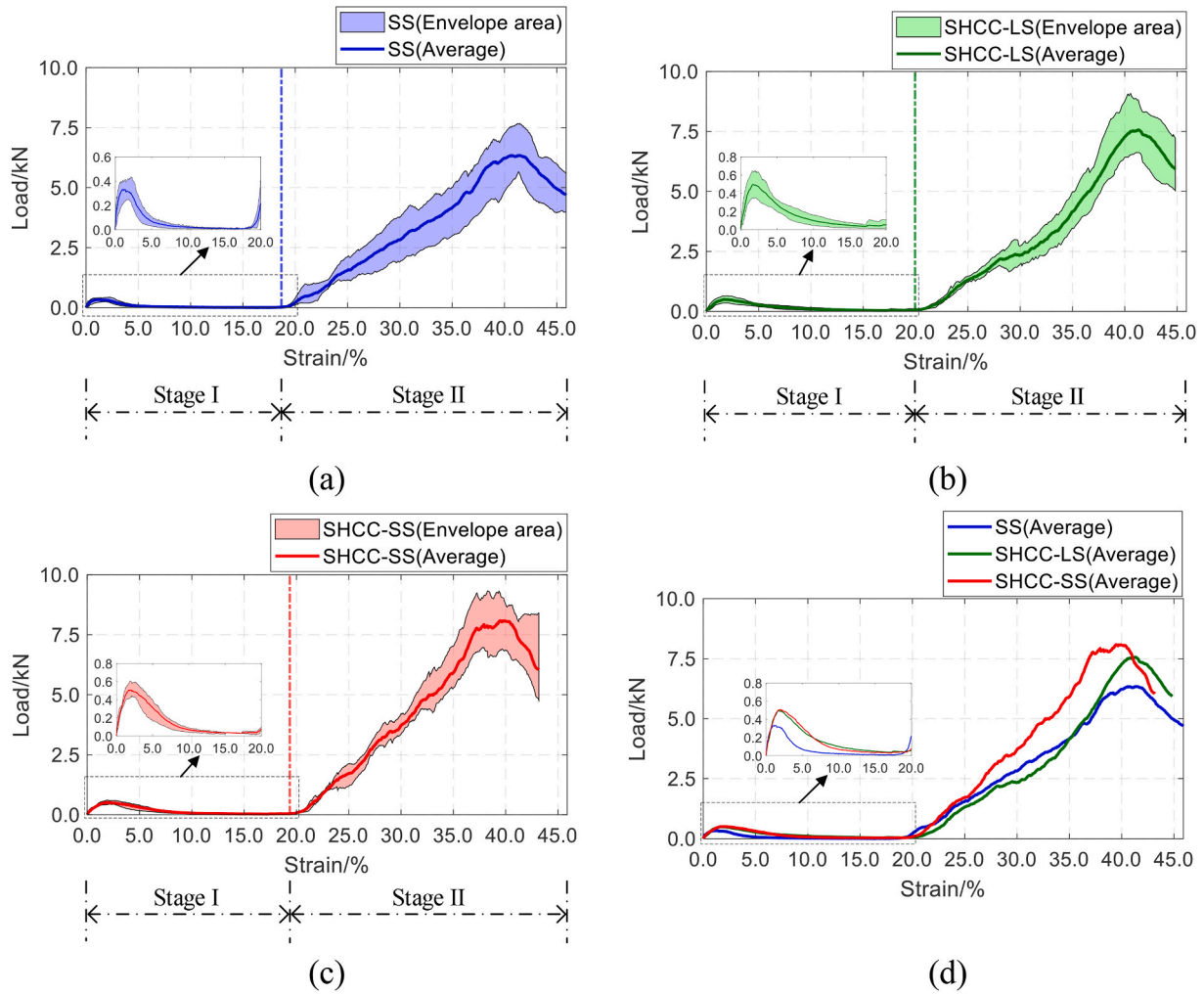


Fig. B1. Load-strain curve of ACCCs under uniaxial compression, (a) ACCCs using SS, (b) ACCCs using SHCC-LS, (c) ACCCs using SHCC-SS, (d) comparison of the three mixtures.

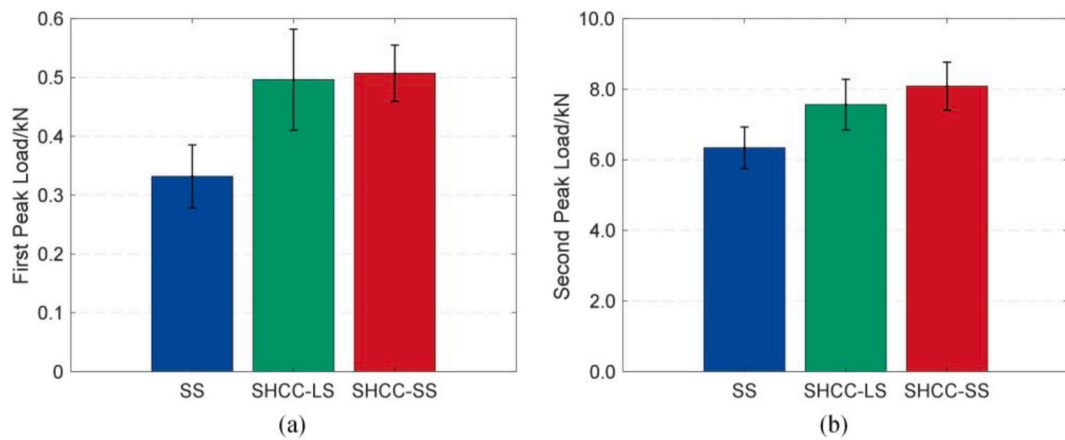


Fig. B2. Comparison of a) the first peak load, (b) the second peak load. (Error bars in all plots indicate standard deviation.)

Table B1
Comparison of the first peak load and the second peak load.

Mixture	First peak load (kN)	Second peak load (kN)
SS	0.332 ± 0.054	6.340 ± 0.591
SHCC-LS	0.496 ± 0.086	7.565 ± 0.716
SHCC-SS	0.507 ± 0.048	8.086 ± 0.680

Appendix C. Mechanical analysis for the hinge joints in ACCCs

The mechanical analysis of the hinge joints in ACCCs is illustrated in Fig. C1. This analysis is limited to the initial moment, during which the structure is in the elastic deformation phase. The shape of the ACCCs is characterized by the geometric parameters a_0 (half major axis) and b_0 (half minor axis), with O denoting the central point. The equilibrium equations, including both force equilibrium equations and moment equilibrium equations, are established using the following formulas. F refers to force; M refers to moment. The labels x and y represent the coordinate axis directions, while J denotes the joint. h is the size of joint in the x - y plane. t is the thickness of ACCCs in the z direction. Considering the symmetry, the mechanical analysis can be simplified to focus on 1/4 of the structure.

The force equilibrium equations in the y direction is

$$F_{1y} = F_{5y} \tag{C1}$$

The force equilibrium equations in the x direction is

$$F_{2x} = F_{5x} \tag{C2}$$

The moment equilibrium equations can be formulated as

$$M_1 + M_2 + F_{2x} \cdot (a_0 + h/2) = F_{1y} \cdot (a_0 - b_0) \tag{C3}$$

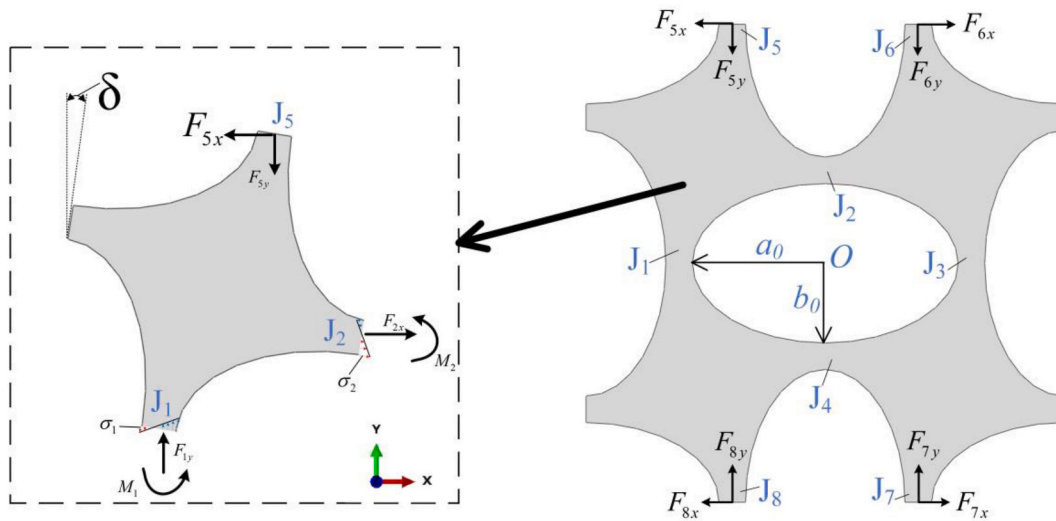


Fig. C1. Mechanical analysis for the hinge joints in ACCCs

The rotation of ACCCs primarily results from the deformation at the four points located at the top (J_2), bottom (J_4), left (J_1), and right (J_3). The deformation of other parts of the structure is minimal and can be considered as rigid body motion relative to the joint. Since 1/4 of the structure exhibits rotational symmetry, when the structure rotates by a small angle δ , the angular deformations at J_2 and J_1 are consistent, specifically δ_1 and δ_2 , respectively.

$$\delta_1 = \delta_2 = \int \kappa ds \tag{C4}$$

where κ is the curvature at the joint and ds is the infinitesimal arc length of the deformation segment at the joint. Since the elastic deformation segment s of the cementitious material is very small and the two joints (J_2 and J_1) have the same geometry, s and κ can be considered constant at the joint.

$$\delta_1 = \delta_2 = \kappa s \tag{C5}$$

The two joints (J_2 and J_1) have the same moment of inertia due to their identical geometries.

$$I = \frac{th^3}{12} \tag{C6}$$

Based on the relationship between bending moment and curvature, the following can be inferred:

$$M_1 = M_2 = EI\kappa \quad (C7)$$

Then, the edge stress on the tensile side of joint J_1 can be expressed as:

$$\sigma_1 = \frac{M_1 h}{I} - \frac{F_{1y}}{th} \quad (C8)$$

Then, the edge stress on the tensile side of joint J_2 can be expressed as:

$$\sigma_2 = \frac{M_2 h}{I} + \frac{F_{2x}}{th} \quad (C9)$$

It is worth noting that the pressure F_{5y} on joint J_5 is related to its frictional force F_{5x} by the following equation:

$$F_{5x} = \mu F_{5y} \quad (C10)$$

where μ is the coefficient of friction.

Finally, by combining Eqs. C1, C2, C6, C7, C8, and C9, the following result can be obtained:

$$\sigma_1 = \frac{(6M_1 - hF_{5y})}{th^2} \quad (C11)$$

$$\sigma_2 = \frac{(6M_1 + \mu hF_{5y})}{th^2} \quad (C12)$$

From this, it can be seen from Eqs. C11 and C12 that σ_2 is greater than σ_1 , meaning that the top joint J_2 reaches the yield stress and enters the plastic stage before the left joint J_1 . According to the tensile constitutive behavior of the reference mixture, the joint deformation increases after reaching yield stress and the stress starts to decrease, follow by crack initiation and growth. In contrast, crack in the left joint J_1 develops more slowly. Considering the symmetry of the structure, the left and right joints (J_1, J_3) have a slower crack development compared to that in the top and bottom joints (J_2, J_4).

Appendix D. Optical microscope images of fiber bridging behavior for ACCCs

As shown in Fig. D1, a digital optical microscope was utilized to investigate the fiber bridging and pull-out behaviors at crack locations within the joints between neighboring holes in ACCC specimens with the three mixtures after cyclic loading. It can be found that the reference (SS) exhibited a single, wide primary crack in the joint, with significant fiber pull-out, twisting, and fracturing at the ends [16]. The primary crack is triangular in shape with a significantly large opening, and its crack tip extends directly to the opposite end. Consequently, it demonstrated the weakest bridging capability and relatively poor recoverable deformation elasticity. Nevertheless, ACCCs with SHCC mixtures display reduced primary crack openings by redistributing deformation across multiple adjacent cracks. As primary cracks develop, their paths change due to fiber bridging and crack merging, resulting in non-angular shapes. The crack tips do not reach the opposite end, leaving some areas intact. Consequently, ACCCs with SHCC mixtures demonstrate improved fiber bridging capability and notable recoverable deformation elasticity. ACCCs made from SHCC-SS show limited fiber bridging within the crack region and fiber breakage near the crack opening due to the sudden failure of the SHCC-SS mixture after reaching its tensile strain capacity (measured in uniaxial tension tests). In contrast, ACCCs using the SHCC-LS mixture exhibit strong fiber bridging within the crack region and fiber pull-out in fewer areas near the crack opening. The SHCC-LS mixture, after reaching its tensile strain capacity, maintains ductility through extended softening enabled by fiber bridging. This explains the higher recoverable deformation elasticity of ACCCs using the SHCC-LS mixture compared to those using the SHCC-SS mixture.

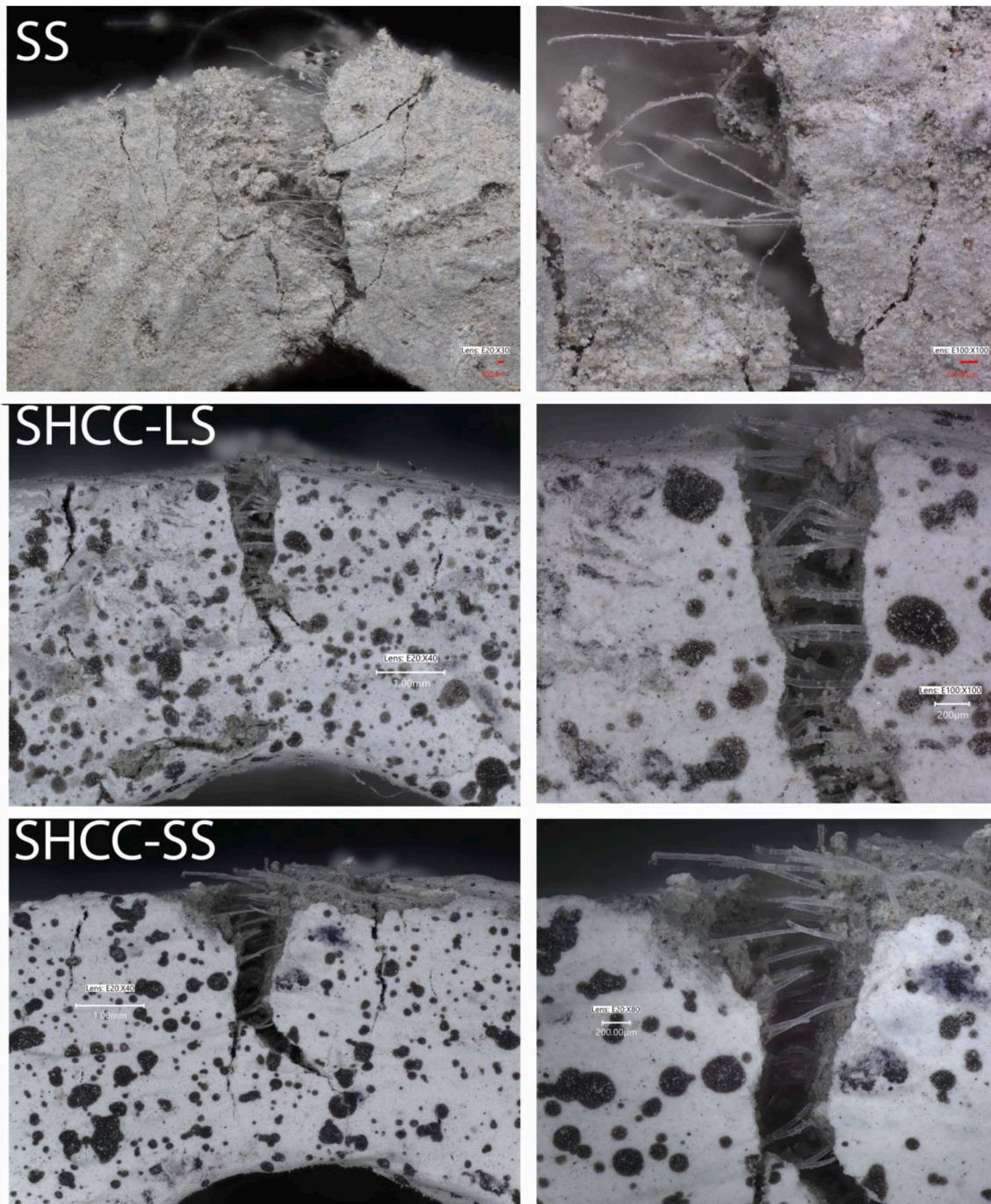


Fig. D1. Optical microscope images of fiber bridging behaviors for ACCCs

Appendix E. Test results of modified P1-shaped ACCCs with increased joint thickness

To validate the advantages of the material proposed in this study, we fabricated and tested another cell type of ACCCs (P1-thick), which features an increased joint thickness based on modifications to the P1-shaped ACCC design shown in Fig. E1. The dimensions of this ACCC shape and the experimental setup for uniaxial compression testing are provided in Fig. E1a and Fig. E1b, respectively. Its thickness in the out-of-plane direction remains 20 mm, the same as that of P1. The increased joint thickness of the P1-thick ACCCs requires a higher fiber-bridging capacity in the cementitious matrix. Fig. E1c displays the stress-strain curves under uniaxial compression for different mixtures. Similarly, ACCCs made from SHCC show superior load-bearing capacity within the high auxetic behavior range under uniaxial compression compared to the reference (SS). In our experiments, only one of the three SS specimens exhibited auxetic behavior, while the other two split under compression. This is because the fiber-bridging capacity of SS does not consistently provide sufficient crack resistance to support section rotation in the thick joints. SS-based ACCCs are more susceptible to additional factors such as manual casting uncertainties, the heterogeneity of cementitious materials, and loading boundary conditions (e.g., friction at the contact surface of specimen-loading plate). In contrast, SHCC-based ACCCs maintain stable auxetic behavior within the

high auxetic behavior range under compression. The susceptibility of SS-based ACCCs to splitting due to these additional factors was also observed in cyclic tests. Fig. E2 illustrates the cyclic behavior of the P1-thick ACCC. Similarly, compared to the reference, ACCCs made from SHCC-LS and SHCC-SS exhibit higher elastic moduli for recoverable deformation. Specially, SHCC-LS demonstrates greater recoverable deformation elasticity than SHCC-SS due to its extended softening, which improves fiber-bridging within the primary cracks in the joints of the P1-thick ACCCs.

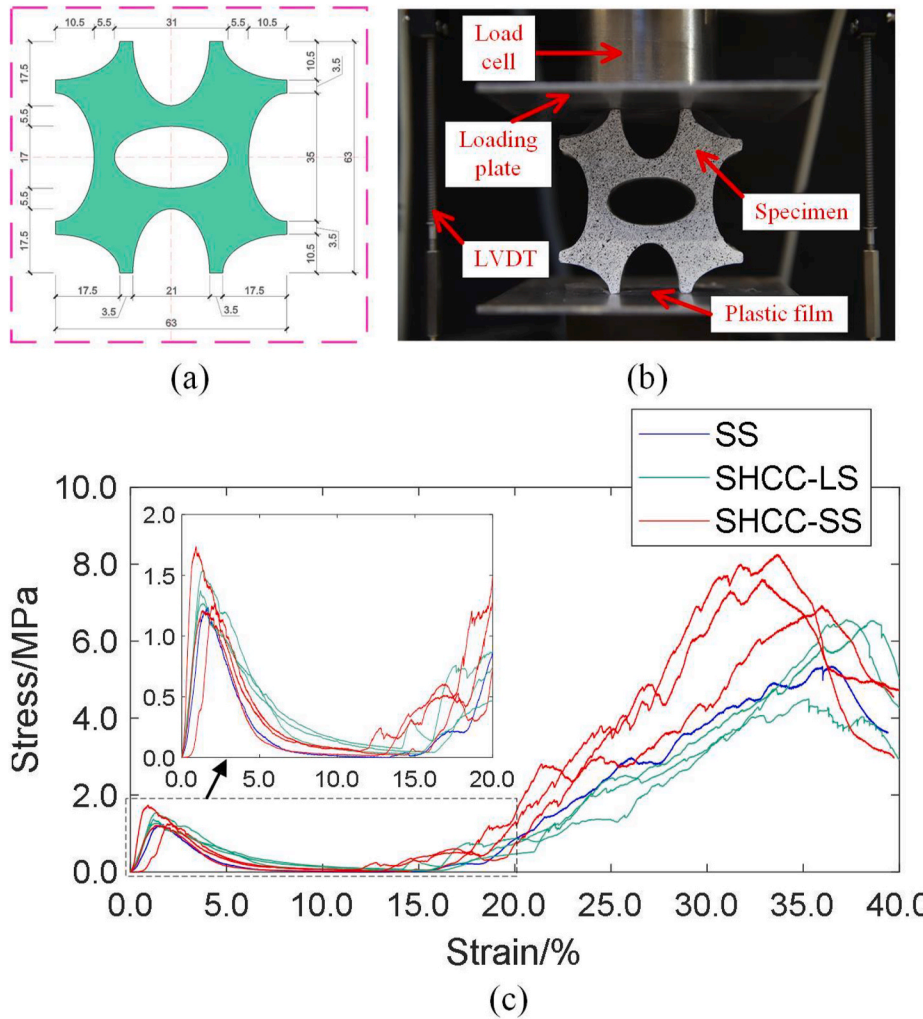


Fig. E1. P1-thick ACCCs, (a) dimensions, (b) experimental setup under uniaxial compression, (c) stress-strain curve under uniaxial compression using different mixtures.

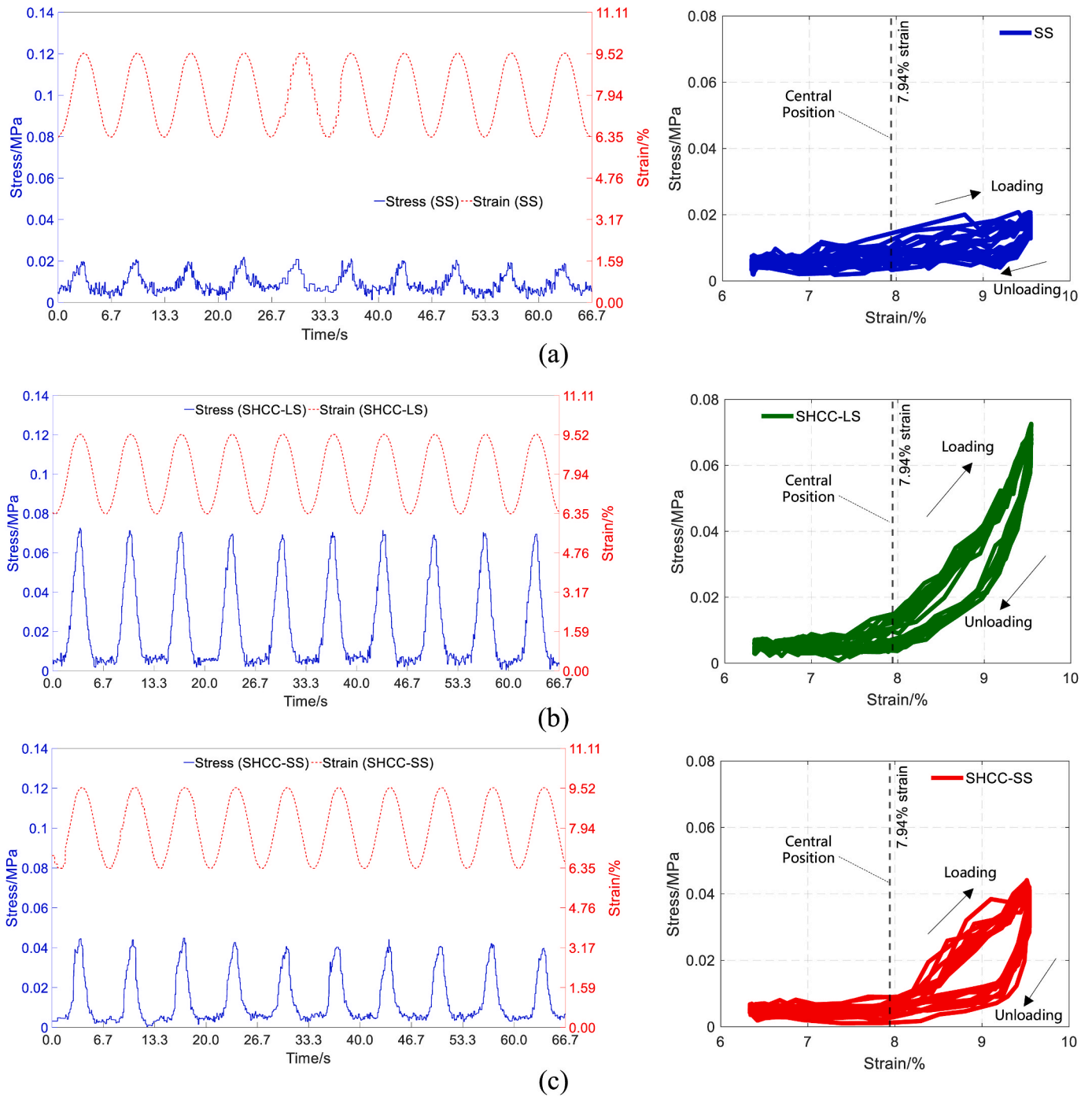


Fig. E2. Cyclic behavior of P1-thick ACCCs, (a) reference (SS), (b) SHCC-LS, (b) SHCC-SS.

Appendix F. Supplementary data

Supplementary data to this article can be found online at <https://doi.org/10.1016/j.cemconcomp.2025.106069>.

Data availability

Data will be made available on request.

References

[1] M. Moini, J. Olek, J.P. Youngblood, B. Magee, P.D. Zavattieri, Additive manufacturing and performance of architected cement-based materials, *Adv. Mater.* 30 (2018) 1802123, <https://doi.org/10.1002/adma.201802123>.
 [2] S.M. Sajadi, C.S. Tiwary, A.H. Rahmati, S.L. Eichmann, C.J. Thaemlitz, D. Salpekar, A.B. Puthirath, P.J. Boul, M.M. Rahman, A. Meiyazhagan, P.M. Ajayan,

- Deformation resilient cement structures using 3D-printed molds, *iScience* 24 (2021) 102174, <https://doi.org/10.1016/j.isci.2021.102174>.
- [3] Z. Wan, Y. Xu, S. He, Y. Chen, J. Xie, B. Šavija, Direct ink writing of vascularized self-healing cementitious composites, *Cement Concr. Compos.* 144 (2023) 105295, <https://doi.org/10.1016/j.cemconcomp.2023.105295>.
- [4] V.C. Li, On engineered cementitious composites (ecc) A review of the material and its applications, *J. Adv. Concr. Technol.* 1 (2003) 215–230, <https://doi.org/10.3151/jact.1.215>.
- [5] J.-X. Zhu, K.-F. Weng, B.-T. Huang, L.-Y. Xu, J.-G. Dai, Ultra-High-Strength Engineered Cementitious Composites (UHS-ECC) panel reinforced with FRP bar/grid: development and flexural performance, *Eng. Struct.* 302 (2024) 117193, <https://doi.org/10.1016/j.engstruct.2023.117193>.
- [6] J.-C. Lao, R.-Y. Ma, L.-Y. Xu, Y. Li, Y.-N. Shen, J. Yao, Y.-S. Wang, T.-Y. Xie, B.-T. Huang, Fly ash-dominated high-strength engineered/strain-hardening geopolymer composites (HS-EGC/SHGC): influence of alkalinity and environmental assessment, *J. Clean. Prod.* 447 (2024) 141182, <https://doi.org/10.1016/j.jclepro.2024.141182>.
- [7] Q.-H. Li, A.-M. Luo, B.-T. Huang, G.-Z. Wang, S.-L. Xu, Bond behavior between steel bar and strain-hardening fiber-reinforced cementitious composites under fatigue loading, *Eng. Struct.* 314 (2024) 118354, <https://doi.org/10.1016/j.engstruct.2024.118354>.
- [8] V.-C. Li, Tailoring ECC for special attributes: a review, *Int. J. Concrete Struct. Mater.* 6 (2012) 135–144, <https://doi.org/10.1007/s40069-012-0018-8>.
- [9] E.-H. Yang, V.C. Li, Tailoring engineered cementitious composites for impact resistance, *Cement Concr. Res.* 42 (2012) 1066–1071, <https://doi.org/10.1016/j.cemconres.2012.04.006>.
- [10] V. Nguyen-Van, J. Liu, S. Li, G. Zhang, H. Nguyen-Xuan, P. Tran, Modelling of 3D-printed bio-inspired Bouligand cementitious structures reinforced with steel fibres, *Eng. Struct.* 274 (2023) 115123, <https://doi.org/10.1016/j.engstruct.2022.115123>.
- [11] J. Liu, S. Li, K. Fox, P. Tran, 3D concrete printing of bioinspired Bouligand structure: a study on impact resistance, *Addit. Manuf.* 50 (2022) 102544, <https://doi.org/10.1016/j.addma.2021.102544>.
- [12] G. Du, Y. Sun, Y. Qian, Flexural performance of nature-inspired 3D-printed strain-hardening cementitious composites (3DP-SHCC) with Bouligand structures, *Cement Concr. Compos.* 149 (2024) 105494, <https://doi.org/10.1016/j.cemconcomp.2024.105494>.
- [13] W. Zhou, W. McGee, H.S. Gökçe, V.C. Li, A bio-inspired solution to alleviate anisotropy of 3D printed engineered cementitious composites (3DP-ECC): knitting/tilting filaments, *Autom. ConStruct.* 155 (2023) 105051, <https://doi.org/10.1016/j.autcon.2023.105051>.
- [14] M. Ohno, M. Pierre, K. Imagawa, T. Ishida, Simulation and learning-driven design for architected cement-based materials, *J. Build. Eng.* 65 (2023) 105768, <https://doi.org/10.1016/j.job.2022.105768>.
- [15] Y. Xu, H. Zhang, E. Schlangen, M. Luković, B. Šavija, Cementitious cellular composites with auxetic behavior, *Cement Concr. Compos.* 111 (2020) 103624, <https://doi.org/10.1016/j.cemconcomp.2020.103624>.
- [16] J. Xie, Y. Xu, Z. Meng, M. Liang, Z. Wan, B. Šavija, Peanut shaped auxetic cementitious cellular composite (ACCC), *Constr. Build. Mater.* 419 (2024) 135539, <https://doi.org/10.1016/j.conbuildmat.2024.135539>.
- [17] Y. Xu, B. Šavija, 3D auxetic cementitious-polymeric composite structure with compressive strain-hardening behavior, *Eng. Struct.* 294 (2023) 116734, <https://doi.org/10.1016/j.engstruct.2023.116734>.
- [18] Y. Xu, B. Šavija, Auxetic cementitious composites (ACCs) with excellent compressive ductility: experiments and modeling, *Mater. Des.* 237 (2024) 112572, <https://doi.org/10.1016/j.matdes.2023.112572>.
- [19] Y. Xu, Z. Meng, R.J.M. Bol, B. Šavija, Spring-like behavior of cementitious composite enabled by auxetic hyperelastic frame, *Int. J. Mech. Sci.* 275 (2024) 109364, <https://doi.org/10.1016/j.ijmecsci.2024.109364>.
- [20] M. Chen, Z. Chen, Y. Xuan, T. Zhang, M. Zhang, Static and dynamic compressive behaviour of 3D printed auxetic lattice reinforced ultra-high performance concrete, *Cement Concr. Compos.* 139 (2023) 105046, <https://doi.org/10.1016/j.cemconcomp.2023.105046>.
- [21] J. Xie, Y. Xu, Z. Wan, A. Ghaderiaram, E. Schlangen, B. Šavija, Auxetic cementitious cellular composite (ACCC) PVDF-based energy harvester, *Energy Build.* 298 (2023) 113582, <https://doi.org/10.1016/j.enbuild.2023.113582>.
- [22] K. Barri, Q. Zhang, J. Kline, W. Lu, J. Luo, Z. Sun, B.E. Taylor, S.G. Sachs, L. Khazanovich, Z.L. Wang, A.H. Alavi, Multifunctional nanogenerator-integrated metamaterial concrete systems for smart civil infrastructure, *Adv. Mater.* 35 (2023) 2211027, <https://doi.org/10.1002/adma.202211027>.
- [23] D. Valverde-Burneo, N. García-Troncoso, I. Segura, M. García-Laborda, Multifunctional cementitious composite: conductive and auxetic behavior, *Case Stud. Constr. Mater.* 20 (2024) e03358, <https://doi.org/10.1016/j.cscm.2024.e03358>.
- [24] S. He, Y. Chen, M. Liang, E.-H. Yang, E. Schlangen, Distribution of porosity surrounding a microfiber in cement paste, *Cement Concr. Compos.* 142 (2023) 105188, <https://doi.org/10.1016/j.cemconcomp.2023.105188>.
- [25] A.M. Tawfek, Z. Ge, H. Yuan, N. Zhang, H. Zhang, Y. Ling, Y. Guan, B. Šavija, Influence of fiber orientation on the mechanical responses of engineering cementitious composite (ECC) under various loading conditions, *J. Build. Eng.* 63 (2023) 105518, <https://doi.org/10.1016/j.job.2022.105518>.
- [26] Y. Gan, M. Liang, E. Schlangen, K. van Breugel, B. Šavija, Two scale models for fracture behaviours of cementitious materials subjected to static and cyclic loadings, *Constr. Build. Mater.* 426 (2024) 136107, <https://doi.org/10.1016/j.conbuildmat.2024.136107>.
- [27] J. Sun, J. Xie, Y. Zhou, Y. Zhou, A 3D three-phase meso-scale model for simulation of chloride diffusion in concrete based on ANSYS, *Int. J. Mech. Sci.* 219 (2022) 107127, <https://doi.org/10.1016/j.ijmecsci.2022.107127>.
- [28] C. Li Victor, K.Y. Leung Christopher, Steady-state and multiple cracking of short random fiber composites, *J. Eng. Mech.* 118 (1992) 2246–2264, [https://doi.org/10.1061/\(ASCE\)0733-9399\(1992\)118:11\(2246\)](https://doi.org/10.1061/(ASCE)0733-9399(1992)118:11(2246)).
- [29] D.B. Marshall, B.N. Cox, A J-integral method for calculating steady-state matrix cracking stresses in composites, *Mech. Mater.* 7 (1988) 127–133, [https://doi.org/10.1016/0167-6636\(88\)90011-7](https://doi.org/10.1016/0167-6636(88)90011-7).
- [30] S. Zhang, V.C. Li, G. Ye, Micromechanics-guided development of a slag/fly ash-based strain-hardening geopolymer composite, *Cement Concr. Compos.* 109 (2020) 103510, <https://doi.org/10.1016/j.cemconcomp.2020.103510>.
- [31] T. Kanda, V.C. Li, Practical design criteria for saturated pseudo strain hardening behavior in ECC, *J. Adv. Concr. Technol.* 4 (2006) 59–72, <https://doi.org/10.3151/jact.4.59>.
- [32] B. Nematollahi, J. Sanjayan, F.U.A. Shaikh, Matrix design of strain hardening fiber reinforced engineered geopolymer composite, *Compos. B Eng.* 89 (2016) 253–265, <https://doi.org/10.1016/j.compositesb.2015.11.039>.
- [33] Y. Xu, E. Schlangen, M. Luković, B. Šavija, Tunable mechanical behavior of auxetic cementitious cellular composites (CCCs): experiments and simulations, *Constr. Build. Mater.* 266 (2021) 121388, <https://doi.org/10.1016/j.conbuildmat.2020.121388>.
- [34] C.-C. Hung, Y.-F. Su, Y.-M. Su, Mechanical properties and self-healing evaluation of strain-hardening cementitious composites with high volumes of hybrid pozzolan materials, *Compos. B Eng.* 133 (2018) 15–25, <https://doi.org/10.1016/j.compositesb.2017.09.005>.
- [35] Y.-F. Su, R.R. Kotian, N. Lu, Energy harvesting potential of bendable concrete using polymer based piezoelectric generator, *Compos. B Eng.* 153 (2018) 124–129, <https://doi.org/10.1016/j.compositesb.2018.07.018>.
- [36] J. Xie, Y. Xu, Z. Wan, A. Ghaderiaram, E. Schlangen, B. Šavija, Modelling of energy harvesting with bendable concrete and surface-mounted PVDF, *Smart Mater. Struct.* 33 (2024) 085008, <https://doi.org/10.1088/1361-665X/ad43cb>.
- [37] S. He, S. Mustafa, Z. Chang, M. Liang, E. Schlangen, M. Luković, Ultra-thin Strain Hardening Cementitious Composite (SHCC) layer in reinforced concrete cover zone for crack width control, *Eng. Struct.* 292 (2023) 116584, <https://doi.org/10.1016/j.engstruct.2023.116584>.
- [38] W. Zhou, Y. Zhang, L. Ma, V.C. Li, Influence of printing parameters on 3D printing engineered cementitious composites (3DP-ECC), *Cement Concr. Compos.* 130 (2022) 104562, <https://doi.org/10.1016/j.cemconcomp.2022.104562>.
- [39] K. Tosun-Felekoğlu, B. Felekoğlu, R. Ranade, B.Y. Lee, V.C. Li, The role of flaw size and fiber distribution on tensile ductility of PVA-ECC, *Compos. B Eng.* 56 (2014) 536–545, <https://doi.org/10.1016/j.compositesb.2013.08.089>.
- [40] K. Rokugo, T. Kanda, H. Yokota, N. Sakata, Applications and recommendations of high performance fiber reinforced cement composites with multiple fine cracking (HPFRCC) in Japan, *Mater. Struct.* 42 (2009) 1197–1208, <https://doi.org/10.1617/s11527-009-9541-8>.
- [41] A. Alomarah, Y. Yuan, D. Ruan, A bio-inspired auxetic metamaterial with two plateau regimes: compressive properties and energy absorption, *Thin-Walled Struct.* 192 (2023) 111175, <https://doi.org/10.1016/j.tws.2023.111175>.
- [42] S. Duan, W. Wen, D. Fang, Additively-manufactured anisotropic and isotropic 3D plate-lattice materials for enhanced mechanical performance: simulations & experiments, *Acta Mater.* 199 (2020) 397–412, <https://doi.org/10.1016/j.actamat.2020.08.063>.
- [43] A.B.M. Supian, S.M. Sapuan, M.Y.M. Zuhri, E.S. Zainudin, H.H. Ya, Hybrid reinforced thermoset polymer composite in energy absorption tube application: a review, *Defence Technol.* 14 (2018) 291–305, <https://doi.org/10.1016/j.dt.2018.04.004>.
- [44] M. Ketabdari, E. Toraldo, M. Crispino, V. Lunkar, Evaluating the interaction between engineered materials and aircraft tyres as arresting systems in landing overrun events, *Case Stud. Constr. Mater.* 13 (2020) e00446, <https://doi.org/10.1016/j.cscm.2020.e00446>.